Studia Quaternaria, vol. 43 (2026): 75–93
DOI: 10.24425/sq.2026.158732

A MULTI-PROXY APPROACH TO DOSE RATE DETERMINATION AT THE KOWALEWO AND BARANÓWKO SITES, POLAND

Agnieszka Szymak[1*], Konrad Tudyka[1], Piotr Moska[1], Robert Jan Sokołowski[2], Andrzej Wojtalak[1], Grzegorz Poręba[1], Piotr Kenis[3]

[1] *Institute of Physics - Centre for Science and Education, Silesian University of Technology, Konarskiego 22B, 44-100 Gliwice, Poland; e-mails: AS Agnieszka.Szymak@polsl.pl, KT Konrad.Tudyka@polsl.pl, PM Piotr.Moska@polsl.pl, AW Andrzej.Wojtalak@polsl.pl, GP Grzegorz.Poreba@polsl.pl*

[2] *Department of Geophysics, Institute of Oceanography, University of Gdańsk, al. Piłsudskiego 46, 81-378 Gdynia, Poland; e-mail: Robert.Sokolowski@ug.edu.pl*

[3] *PORT Polish Center for Technology Development, Stabłowicka 147, 54-066 Wrocław, Poland; e-mail: Piotr.Kenis@port.lukasiewicz.gov.pl*

* *corresponding author*

Abstract:

This study evaluates dose rate determination for Optically Stimulated Luminescence (OSL) dating of aeolian sediments by investigating the origin and variability of external and internal dose rate components. Three independent radioactivity measurement techniques: High-Purity Germanium (HPGe) gamma spectrometry, ICP-MS - Inductively Coupled Plasma Mass Spectrometry and the μDOSE system were compared using samples from two contrasting dune successions in Poland: Kowalewo (fluvio-aeolian–aeolian) and Baranówko (aeolian). Elevated radionuclide activity was detected in quartz separates prior to HF treatment, particularly in the Kowalewo profile, indicating that radionuclide-bearing material may remain associated with density-separated quartz. HF treatment reduced this activity; however, after conversion to dose rate, the internal quartz component represented only a minor contribution to the total environmental dose rate under the investigated conditions. To explain the observed dose rate variability, results from automated mineralogical analysis (QEMSCAN® - Quantitative Evaluation of Minerals by Scanning Electron Microscopy), conventional heavy-mineral analysis, quartz-grain morphoscopy and Principal Component Analysis (PCA) were interpreted together. QEMSCAN® was used to identify the principal mineral hosts of radionuclides, whereas conventional heavy-mineral analysis and quartz-grain morphoscopy were used to characterise sediment provenance, maturity and transport history. The complementary datasets show that U and Th activities are primarily associated with accessory radionuclide-bearing mineral phases identified by QEMSCAN®, whereas K activity is mainly related to K-feldspar and fine-grained aluminosilicates recognised by QEMSCAN®. Conventional heavy-mineral analysis and quartz-grain morphoscopy provide independent evidence that differences in provenance, sediment maturity and transport history between the two sedimentary successions influence radionuclide partitioning within the sediment matrix and the response of quartz separates to HF treatment. Although these effects have only a limited influence on the total environmental dose rate in the investigated sediments, integrating dosimetric measurements with complementary mineralogical and sedimentological evidence provides a more robust framework for interpreting radionuclide distribution and assessing dose rates for OSL dating.

Key words: Luminescence dating; Internal dose rate; Quartz; Dose rate.

Manuscript received 25 May 2026, accepted 10 July 2026

INTRODUCTION

In OSL dating, a significant part of the literature has focused on methodological developments related to equivalent dose determination. These studies are primarily aimed at improving the accuracy and precision of equivalent dose estimates. By comparison, aspects related to dose rate determination and its associated uncertainties have received comparatively less attention, particularly in the context of complex sediment mineralogy and microdosimetric heterogeneity (Murray *et al*., 2018). From the perspective of obtaining reliable age estimates, accurate dose rate determination remains essential. The calculated dose rate depends not only on metrological accuracy but also on the geological and mineralogical characteristics of the studied sediment. In particular, unresolved issues related to microdosimetric effects and the distribution of radionuclide-bearing mineral phases may influence dose rate estimates. For example, in some low-radioactivity profiles, dose rates may be slightly underestimated if internal dose rate contributions are neglected (Szymak *et al*., 2022).

In this study, we address uncertainty in dose rate determination arising from the heterogeneous distribution of radionuclides within the sediment matrix and their association with different mineral phases and grain surfaces. In particular, we investigate how radionuclide partitioning among accessory mineral phases, fine fractions and quartz grain surfaces influences dose rate estimates in aeolian sediments.

To investigate these processes, three complementary methods of natural radioactivity determination were applied to evaluate inter-method agreement and identify potential systematic differences in dose rate estimation. In addition, automated mineralogical analysis (QEMSCAN®) was used to identify the principal mineral phases that host radionuclides and to characterise their distribution within the sediment matrix. Conventional heavy-mineral analysis and quartz-grain morphoscopy were employed independently to characterise sediment composition, provenance, transport history and sediment maturity. Together, these complementary datasets provide a multi-proxy framework in which each method addresses a different aspect of the sedimentary system: environmental radioactivity (HPGe gamma spectrometry, ICP-MS and μDOSE), radionuclide-hosting mineral phases (QEMSCAN®), bulk heavy-mineral assemblages (conventional heavy-mineral analysis), and quartz-grain surface textures (morphoscopy). Their integration allows relationships between sedimentary history, mineralogical characteristics and dose rate to be evaluated while recognising that the different datasets provide complementary rather than directly equivalent information.

The study is guided by the following testable hypotheses: (i) radionuclide activities determined by HPGe gamma spectrometry, ICP-MS and μDOSE agree within analytical uncertainty, indicating methodological comparability; (ii) hydrofluoric acid (HF) treatment reduces apparent radionuclide activity in quartz separates by removing surface-associated contaminants and/or residual non-quartz mineral phases; (iii) uranium and thorium activities covary with accessory mineral phases identified by QEMSCAN® that are interpreted as the principal hosts of these radionuclides, whereas potassium activity is primarily associated with K-feldspar and fine-grained aluminosilicates. In contrast, conventional heavy-mineral assemblages are expected to reflect sediment provenance and maturity rather than directly identify radionuclide-hosting phases; and (iv) the magnitude of the quartz-associated dose component differs between the Kowalewo and Baranówko profiles as a consequence of their contrasting sedimentary histories and degrees of aeolian reworking.

These hypotheses provide the basis for evaluating whether mineralogical heterogeneity and radionuclide partitioning introduce systematic differences into environmental dose rate determination and, consequently, influence OSL chronostratigraphic interpretation.

The primary objectives of this study are to: (i) quantify inter-method agreement between different radionuclide measurement techniques used for dose rate determination; (ii) assess the origin and variability of external and internal dose rate components and evaluate whether radionuclide-bearing material associated with quartz has a measurable influence on the total environmental dose rate; and (iii) identify the principal mineralogical controls on radionuclide distribution using automated mineralogical analysis (QEMSCAN®), and integrate these observations with conventional heavy-mineral analysis and quartz-grain morphoscopy to distinguish radionuclide-hosting mineral phases from broader indicators of sediment provenance and sediment maturity. OSL dating is subsequently used as an application of the resulting dose rate framework to evaluate the implications of improved dosimetric characterisation for the chronostratigraphic interpretation of the studied aeolian (Baranówko) and fluvio-aeolian–aeolian (Kowalewo) successions.

The Kowalewo and Baranówko sites were selected as contrasting sedimentary systems representing different geomorphic settings, depositional histories and degrees of aeolian reworking, while sharing a broadly comparable regional climatic and sedimentary framework. This enables evaluation of how contrasting sedimentary histories influence radionuclide distribution, dose rate determination and, ultimately, OSL chronostratigraphic interpretation.

STUDY AREA AND REGIONAL SETTING

Kowalewo site

The Kowalewo site is located in the western part of Kujawy, central-western Poland, between the towns of Szubin and Żnin (Fig. 1B). The study area is located in the glacial zone of the last glaciation near the southern edge of the Toruń-Eberswalde Ice-Marginal Valley (IMV; Pisarska-Jamroży, 2015; Marks *et al*., 2023). The exposure of aeolian sediments is located on the leeward side of a

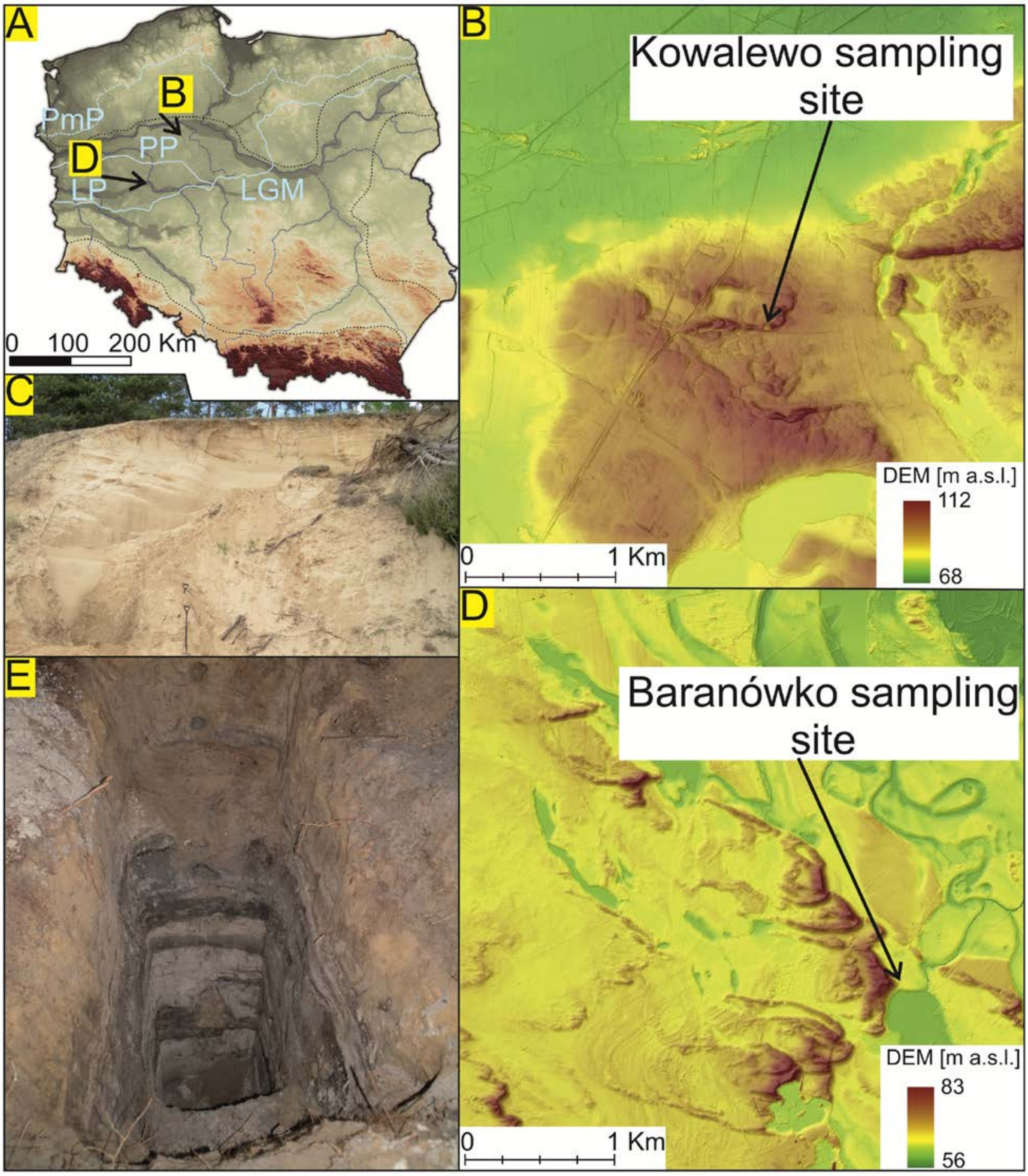

Fig. 1. Location of the study area and sampling sites. Map of Poland showing the general locations of the Kowalewo and Baranówko sites (A) (PmP – Pomeranian Phase, PP – Poznań Phase, LGM – Last Glacial Maximum, LP – Leszno Phase). Detailed location map (B) and a photograph of the investigated profile at the Kowalewo site (C). Detailed location map (D) and a photograph of the investigated profile at the Baranówko site (E).

parabolic dune up to 10 m high (Fig. 1C), situated on a fragment of a moraine plateau isolated by subglacial channels. The substrate of the aeolian sediments consists of fluvial sands and glacial clay originating from the main stage of the last glaciation. The thickness of Quaternary sediments in Kowalewo reaches 18–20 metres. Quaternary formations are underlain by clays and silts of the Miocene Poznań Formation (Włodek, 2002).

Baranówko site

The Baranówko site is located in central Wielkopolska region, central-western Poland (Fig. 1D). It is situated in a complex parabolic dune up to 17 m high, in the northern part of the Śrem Basin (Solon *et al*., 2018), which is part of the middle valley of the Warta River on the terrace IV. The studied outcrop, with a thickness of over 3 m (Fig. 1E), is located on the leeward slope of the dune near the overgrown shore of a lake near the village of Baranówko.

The study area is located in the glacial zone of the last glaciation, approximately 40 km north of the Last Glacial Maximum (LGM) (Wysota *et al.*, 2009; Marks *et al.*, 2022). This area began to form as a result of subglacial erosion processes, the remnants of which are traces of subglacial channels in the Śrem Basin. It was then remodelled as a result of meltwater and extraglacial water flow during the deglaciation of western Poland after the Leszno Phase as part of the Warsaw-Berlin IMV (Kozarski, 1988, 1995). From the termination of the last glaciation until the Holocene, the Śrem Basin functioned as part of the Warta River valley. During this period, a complex of river terraces was formed (Gonera and Kozarski, 1987; Antczak-Górka, 1995). On terrace IV, starting from the beginning of the Late Glacial, the surface was transformed by aeolian processes, resulting in the formation of sandy covers and complex parabolic dunes. These were the subject of studies at the nearby (approximately 900 m to the SW) Żabinko site (Nowaczyk, 1986; Bohncke *et al*., 1995; Zieliński *et al*., 2011; Szymak *et al*., 2024). The studied dune is directly underlain by sandy-gravel deposits of the terrace IV, approximately 10 m thick, below which there are clay and silt of the Poznań Formation of the Miocene age (Nowak, 2001).

Despite these differences in geomorphic setting, stratigraphic architecture and depositional history, both study sites are located within the same regional Late Quaternary sedimentary system of central-western Poland and are characterised by aeolian reworking of sandy material derived primarily from glaciofluvial and fluvial deposits. The Kowalewo and Baranówko profiles therefore represent contrasting expressions of dune development within a broadly comparable climatic and sediment source framework. This allows their comparison in terms of sedimentary processes, mineralogical maturity and radionuclide distribution, while explicitly accounting for differences in geomorphic evolution and post-depositional modification.

MATERIALS AND METHODS

Sampling

Prior to sample collection, lithofacial analysis of the exposed areas was performed in accordance with the methodology proposed by Zieliński and Issmer (2008) to ensure that material was selected from representative lithofacies Kowalewo and Baranówko Sampling was conducted at two primary locations: a 10 m thick profile exposed in a sand pit at the Kowalewo site (Fig. 1C) and a 3.2 m thick profile within a trench at the Baranówko site (Fig. 1E). From each profile, eight samples were collected in lightproof tubes for OSL dating. In addition, bulk material from the same positions was collected in plastic bags for a for ICP-MS, µDOSE, QEMSCAN®, grain size, rounding, and frosting. Additionally, material for radiocarbon dating was collected from the Baranówko profile; however, no suitable organic matter for this purpose was found at the Kowalewo site.

Determination of luminescence age

Equivalent dose determination

The isolation of pure quartz grains for luminescence dating involved a multi-stage chemical pretreatment and mineral separation process. First, they were immersed in 20% hydrochloric acid to remove carbonates, followed by immersion in 20% hydrogen peroxide to eliminate organic matter, with rinsing in distilled water between the steps. After the initial preparation, the samples were dried and sieved using 125–200 µm meshes. Quartz grains were then separated using sodium polytungstate heavy liquids with densities of 2.62 and 2.75 g·cm^{-3}. Subsequently, the grains were etched in 40% hydrofluoric acid for 1 hour to remove an outer layer of approximately 4 µm (Poręba *et al.*, 2022) to eliminate any non-quartz components. Finally, the prepared samples were mounted on stainless steel disks and subjected to luminescence measurement.

Luminescence measurements were carried out using a Risø TL/OSL DA-20 automated reader equipped with a calibrated ^{90}Sr/^{90}Y beta source and Hoya U-340 filter. During the calibration process, Riso quartz was used (Autzen *et al.*, 2022). Equivalent doses were determined using the Single-Aliquot Regenerative-dose (SAR) protocol (Murray and Wintle, 2000), and for each sample, the final equivalent dose was calculated by applying the Central Age Model (CAM) or Minimum Age Model (MAM) (Galbraith *et al*., 1999) using R package 'Luminescence' (Kreutzer *et al*., 2020).

Dose rate determination

Dose rate determination was based on radionuclide concentrations measured in both bulk sediment and extracted quartz grains. For bulk sediment measurements, samples were dried in a laboratory oven at 70°C until their mass stabilized. The dried material was then pulverized, placed in γ-beakers (Poręba *et al*., 2020; Tudyka *et al*., 2021), and stored for a minimum of three weeks to allow ^{222}Rn to reach radioactive equilibrium with ^{226}Ra. Each sample was measured for approximately 48 hours (Moska, 2019).

External dose rates were determined from radionuclides belonging to the ^{238}U and ^{232}Th decay series and from ^{40}K using high-resolution HPGe gamma spectrometry. The HPGe detector was calibrated using IAEA reference materials: IAEA-RGU-1, IAEA-RGTh-1, and IAEA-RGK-1. The activity of the ^{238}U decay series was evaluated based on gamma emissions from its progeny: 63 keV from ^{234}Th, 186 keV from ^{226}Ra, 295 and 352 keV from ^{214}Pb, and 609, 1120, and 1764 keV from ^{214}Bi. For the ^{232}Th decay series, activities were determined from the 338 and 911 keV emissions of ^{228}Ac and the 583 and 2613 keV emissions of ^{208}Tl. The activity of ^{40}K was determined using its characteristic

1460 keV emission line. The activities of individual radionuclides within both decay series were statistically consistent, indicating the absence of secular disequilibrium. Final ^{238}U and ^{232}Th activities were calculated as weighted averages of their respective daughter nuclides.

Bulk material from each sample was additionally analysed using ICP-MS with lithium borate fusion at Bureau Veritas Mineral Laboratories (Canada). Before analysis, samples were dried and ground using a planetary mill. Detection limits were 0.1 ppm for U, 0.2 ppm for Th, and 0.01% for K_2O, and the obtained concentrations were converted to $Bq \cdot kg^{-1}$ (Guérin et al., 2011). Bureau Veritas Mineral Laboratories estimates analytical precision at 15% for concentrations exceeding ten times the detection limit and 100% for concentrations equal to or below the detection limit. The latter uncertainty was estimated using a power-law relationship based on the ICP-MS detection limit (Thompson *et al*., 2002).

Radionuclide concentrations were also measured using the µDOSE system (Tudyka *et al*., 2018, 2020; Kolb *et al*., 2022). This method enables detection of alpha and beta particles and identification of four types of decay pairs originating from the uranium and thorium decay chains, combining the advantages of conventional alpha counting (Aitken, 1985) and beta counting (Bøtter-Jensen and Mejdahl, 1988; Sanderson, 1988) with enhanced radionuclide identification capabilities. Decay pairs were used to determine the specific activities of the uranium and thorium decay chains, whereas residual beta count rates were used to estimate ^{40}K activity. The µDOSE system was calibrated for 3.00 g samples using IAEA reference materials (IAEA-RGU-1, IAEA-RGTh-1, and IAEA-RGK-1) and a mixed reference material containing 1.00 g of each standard. Background levels were evaluated using a 3.00 g polymer disc with negligible radionuclide content.

For internal dose rate determination, quartz grains extracted using the same chemical procedure as described for luminescence dating were analysed. Measurements were performed using the µDOSE system designed for 1.00 g samples. Four analytical variants were prepared: uncrushed and crushed grains after HF treatment, and uncrushed and crushed grains after density separation. The procedure followed the same analytical approach as described above. Additionally, ICP-MS measurements were performed on quartz samples after density separation and after density separation followed by HF etching.

Dose rate calculation

Annual dose rates were calculated using the µRate software (Tudyka *et al*., 2022). To determine the external dose rate, radionuclide concentrations measured by µDOSE, HRGS, and ICP-MS were averaged using a weighted mean. The internal dose rate was calculated based on µDOSE and ICP-MS results of extracted quartz. These specific radioactivity measurements were then used as the basis for calculating the annual dose rate. Several parameters and corrections were applied during the calculation. An a-value of 0.04 ± 0.02 was used. Water content correction was applied following Aitken (1985). For the 125–200 µm quartz fraction, an HF etched layer of 4 ± 2 µm was assumed using values from Bell (1979) and Brennan (2003). Alpha and beta dose attenuation corrections were based on Brennan *et al*. (1991) and Guérin *et al*. (2011), respectively. The cosmic dose rate was estimated according to Prescott and Hutton (1994). Finally, the dose rate used for the age calculation was determined as the sum of the external, internal, and cosmic dose rates.

Radiocarbon dating

For ^{14}C dating four charcoal samples were extracted from the Baranówko profile. No suitable organic remains were found within the Kowalewo profile despite intensive investigation. All recovered samples underwent a standard Acid-Base-Acid pretreatment to eliminate carbonates and humic contaminants. Following pretreatment and graphitization, AMS measurements were made on the MICADAS AMS system (Synal *et al*., 2007) at the Gliwice Radiocarbon and Mass Spectrometry Laboratory. The resulting radiocarbon dates were calibrated with the IntCal20 (Reimer *et al*., 2020) using OxCal 4.4 software (Bronk Ramsey, 2009).

Mineralogical and grain surface analyses

QEMSCAN® measurements

The bulk samples were analysed using the QEMSCAN® system at the Łukasiewicz Research Network – PORT Polish Centre for Technology Development (Wroclaw, Poland). For each sample, the mineral composition of the whole sample, the mineral composition of the granulometric fractions, as well as the mineral associations were determined.

Quantitative mineralogical characterization was performed using a QEMSCAN® system, following analytical protocols commonly applied in previous studies of loess and fine-grained sedimentary materials (Kenis *et al*., 2020; Kenis *et al*., 2025). The method combines automated scanning electron microscopy with energy-dispersive X-ray spectroscopy (SEM-EDS) to obtain quantitative mineralogical, textural, and chemical information at the microscale. Samples were prepared as polished epoxy-mounted sections from homogenized bulk material. The analytical surface was carbon-coated to ensure electrical conductivity. Measurements were conducted under high-vacuum conditions using a field-emission SEM equipped with multiple EDS detectors. Automated measurements were performed using an accelerating voltage of 15 kV, a beam current of 10 nA, and a microscope spot size setting of 4.1, which provided optimal excitation of heavy elements, including rare-earth-element (REE)-bearing phases.

Automated mineral identification was based on the acquisition of EDS spectra at predefined measurement points arranged in a regular grid. Each spectrum was matched against a mineral species identification (MSI) library, allowing assignment of individual pixels to specific mineral phases. The repeatability of the QEMSCAN® analysis was controlled through standardized instrument calibration procedures and the use of a validated MSI database. Previous studies have demonstrated that automated mineralogical analyses performed under stable operating conditions provide highly reproducible modal mineralogical data, particularly for major mineral phases (Pirrie and Rollinson, 2011; Schulz *et al*., 2020).

Mineral phases that were difficult to identify, exhibited disturbed compositions, or yielded ambiguous automated classifications were additionally verified by manual SEM–EDS point analyses performed at accelerating voltages of 15–25 kV and microscope spot size settings ranging from 3.5 to 6.0. The obtained spectra were interpreted using both the MSI database and published reference data (Reed, 2005; Severin, 2004).

Due to intrinsic limitations of the QEMSCAN® technique, clay minerals as well as phases enriched in light elements (e.g., H, Li, Be, B) may be underestimated or not reliably identified. These limitations result primarily from the low X-ray emission efficiency of light elements and the mixed-phase character of fine-grained clay-rich domains. Therefore, comprehensive characterization of such phases requires complementary analytical techniques.

Grain size analysis

Grain-size analysis was conducted using a Malvern Mastersizer 3000 laser diffractometer. Prior to measurement, organic matter was removed by digestion with H_2O_2. For sample dispersion, sodium hexametaphosphate was added, and the mixtures were mechanically shaken overnight in distilled water (Mason *et al*., 2003). Before analysis, samples were ultrasonicated to ensure complete dispersion of particles. Grain-size distributions were calculated as volume percentages, and grain-size parameters (mean grain size and median grain size) were determined using the Folk and Ward (1957) method.

Conventional heavy mineral analysis

Heavy minerals were identified according to the method described by Mange and Maurer (1992). All samples from the Baranówko and Kowalewo profiles were used for the analysis. The samples were sieved to the 125–250 µm fraction and subjected to density separation using a sodium polytungstate solution with a density of 2.85 $g \cdot cm^{-3}$. For each sample, a minimum of 285 transparent mineral grains were identified and classified into the following groups: AMF (amphibole), PIR (pyroxene), BIO (biotite), CHL (chlorite), EPI (epidote), GRA (garnet), TUR (tourmaline), CYR (zircon), RUT (rutile), TYT (titanite), DYS (kyanite), STA (staurolite), AND (andalusite), SYL (sillimanite), APA (apatite), and TOP (topaz).

Measurement of rounding and frosting

Quartz-grain rounding and surface texture were analysed to reconstruct sediment transport and depositional history. The method combined the classical approach of Cailleux (1942) with later refinements by Krinsley and Doornkamp (1973), Krinsley and Margolis (1969), Mahaney (2002), Mycielska-Dowigałło and Woronko (1998). Grain surface characteristics were assessed under reflected-light microscopy and classified as NU (non-used), EL (shiny rounded), EM/EL (intermediate shiny), RM (matt rounded), EM/RM (intermediate matt), C (cracked/broken), and other grain types, while surface features such as cracks, impact marks, microcracks and frosting were used to support environmental interpretation (Table 1). Matte, frosted grains were interpreted as aeolian, whereas smooth, polished and glossy grains were treated as fluvial in origin.

Principal Component Analysis

To evaluate relationships among radionuclide activities (^{238}U, ^{232}Th, ^{40}K), QEMSCAN® mineral carriers, and physical sediment properties (specific surface area), all values were Z-score standardized prior to Principal Component

Table 1. Morphoscopic evaluation of quartz grains under binocular microscopy: surface features, degree of reshape, and implications for sedimentary environment reconstruction.

Code	Description	Paleoenvironmental meaning
NU	fresh grains, without traces of processing, very poorly rounded	physical weathering; crushing in a glacial environment
EL	shiny grains, well or very well rounded	long-term chemical etching and abrasion; commonly associated with a fluvial environment
EM/EL	shiny grains, with an intermediate degree of roundness	fluvial environment
RM	matt grains, well rounded, with clearly rounded surfaces	long-term abrasion during saltation transport; aeolian environment
EM/RM	grains with dulled edges and corners, intermediately rounded	relatively short-lived influence of the aeolian environment
C	cracked grains, with clearly visible surface damage	frost weathering
Other	grains with varying degrees of roundness, without clear traces of abrasion, or atypical grains	intensive chemical and mechanical weathering / forms difficult to assign unequivocally

Analysis (PCA). Calculations were performed in Python using the scikit-learn, SciPy, and Matplotlib. The resulting PC1–PC2 biplots were used to track correlations.

RESULTS AND DISCUSSION

Reliability of OSL dating and implications of dose-rate variability

The equivalent dose results are presented as relative probability density distributions, and the overdispersion parameter was determined for all analysed samples. For all samples from the Kowalewo profile and for five samples from the Baranówko site, the unimodal character of the dose distributions justified the application of the Central Age Model (CAM) model for equivalent dose estimation. In contrast, the remaining three samples from the Baranówko profile exhibited non-unimodal dose distributions; therefore, the Minimum Age Model (MAM) model was applied for the calculation of the final equivalent dose values (Tables A1a and A1b, Appendix). Fig. 2 presents equivalent dose probability density distributions based on individual aliquots. The equivalent dose values from the Baranówko site (0.32–10.7 Gy) exhibit a broad range, indicating significant variability among the analyzed samples, whereas those from the Kowalewo site (20.4–23.9 Gy) are relatively consistent, reflecting a narrow range and low variability.

The external dose rate results show a good agreement between the different measurement methods (Fig. 3). However, the HRGS method (Tables A2a and A2b; Appendix) yields systematically slightly lower values compared to the other techniques (Tables A3a, A3b, A4a, A4b; Appendix), mainly based on ICP-MS data. (Figs. 3B and C). This underestimation may be attributed to small differences in system calibration, particularly when measuring samples with very low radioactivity levels.

Fig. 4 shows the results of internal dose rate determination for the Baranówko and Kowalewo profiles showing the comparison between ICP-MS and µDOSE methods for grains after density separation and grains after HF treatment (Tables A5a and A5b; Appendix). It can be noted that after HF etching process significant decreases the internal dose rate in Kowalewo while in Baranówko the values remain the same. This difference is largely attributable to the external dose rate, as the quartz grains in the Kowalewo

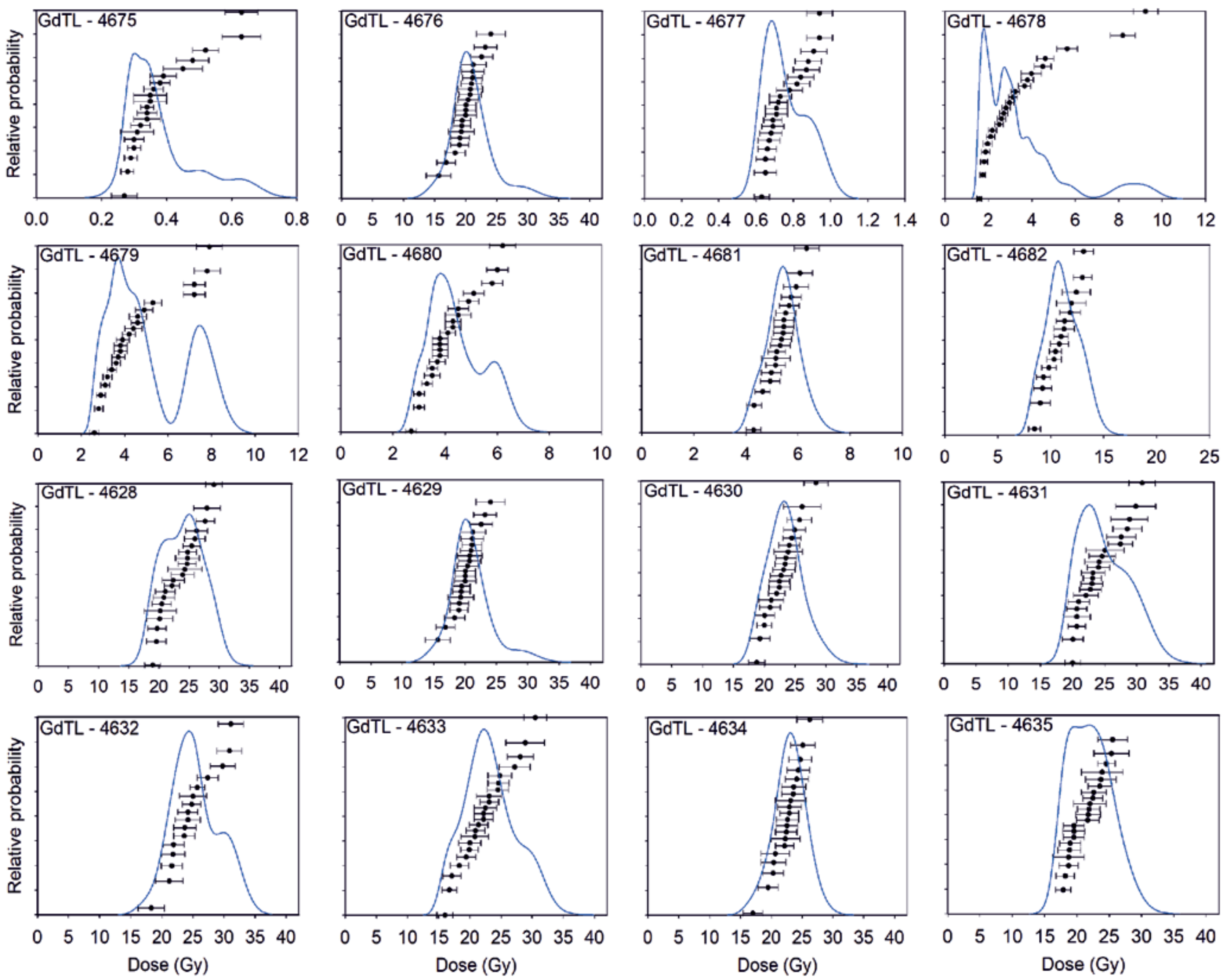

Fig. 2. Probability density plots of equivalent dose values derived from individual aliquots for samples from the Kowalewo and Baranówko sites.

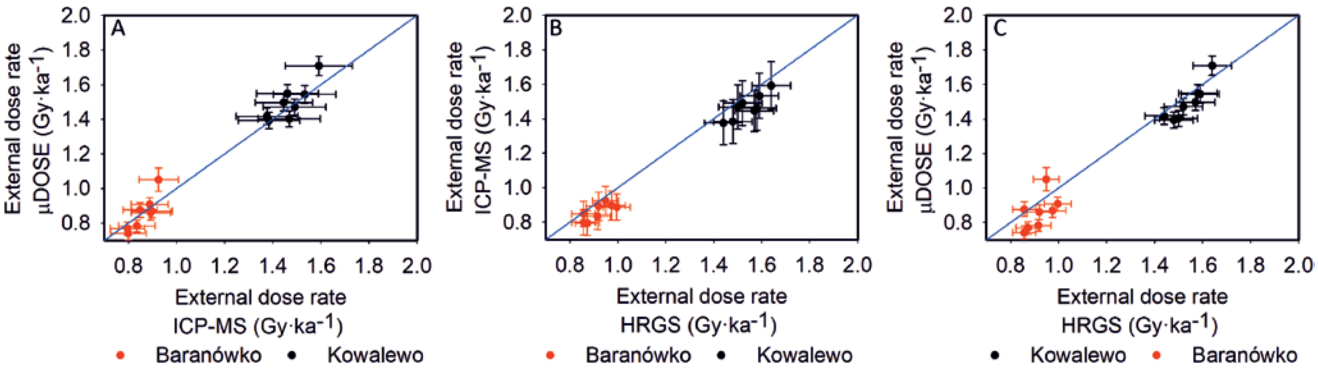

Fig. 3. Results of external dose rate comparison for the Baranówko and Kowalewo profiles presenting correlations between (A) µDOSE and ICP-MS, (B) ICP-MS and HRGS, and (C) µDOSE and HRGS.

profile were situated in a significantly more radioactive environment than those from Baranówko (Fig. 3). Due to this higher environmental radioactivity, a larger number of radionuclides likely accumulated on or near the outer surfaces of the grains or passing through quartz separation steps. The HF etching process effectively removed this external layer or non-quartz grains, leading to the observed decrease in the internal dose rate. In contrast, the lower external radioactivity at the Baranówko site did not result in such surface accumulation, which explains why the HF treatment did not noticeably affect its internal dose values.

The final dose rate is a combination of both external and internal components. However, in both investigated profiles, the internal contribution is very small and does not significantly influence the total final dose rate. Although HF treatment substantially reduced radionuclide activity in quartz separates from the Kowalewo profile, this reduction translated into only a minor change in the total environmental dose rate because the internal quartz component represents only a small fraction of the overall dose. The dosimetric measurements (HPGe gamma spectrometry, ICP-MS and µDOSE) demonstrate the reduction of radionuclide activity in quartz separates following HF treatment. These observations are complemented by automated mineralogical analysis (QEMSCAN®), which identifies the principal mineral hosts of radionuclides, and by conventional heavy-mineral analysis together with quartz-grain morphoscopy, which provide independent information on sediment provenance, maturity and transport history. Interpreted together, these complementary datasets indicate that the effectiveness of HF treatment and the variability of dose-rate components are linked to differences in sediment composition and depositional history rather than to changes in the quartz itself. Consequently, the principal significance of these observations lies in improving our understanding of radionuclide distribution within quartz separates and its implications for dose rate assessment rather than in producing substantial revisions of calculated OSL ages.

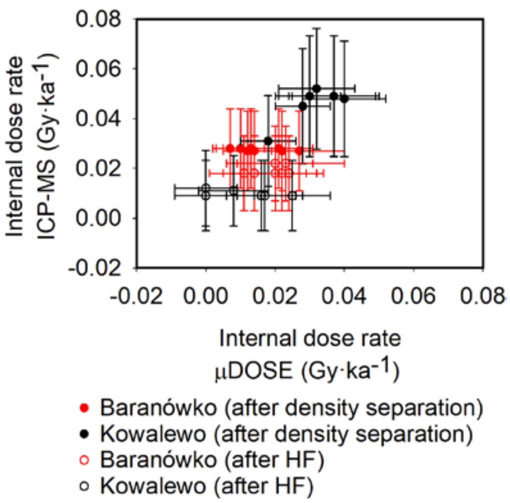

Fig. 4. Results of internal dose rate determination for the Baranówko and Kowalewo profiles showing the comparison between ICP-MS and µDOSE methods for grains after density separation and grains after hydrofluoric acid (HF) treatment.

Sediment provenance and controls on radionuclide distribution

The results of the grain-size distributions for the studied profiles are presented in Fig. 9 (C, C', D and D'). For both studied profiles, the grain-size distributions show that the sediment is composed almost entirely of coarser fractions with only a small contribution of silty fractions, which is typical for this type of sediment (Tables D1a and D2a; Appendix). The Mz and Md values fall within a very narrow range, corresponding mainly to fine sand (Tables D1b and D2b; Appendix). In the profile form Kowalewko at a depth of approximately 350 cm, a slight increase in a finer fraction can be observed; however, the overall profile remains highly uniform. In case Baranówko profile at the base of deposits'(below approximately 290 cm) a shift toward slightly coarser grain size can be observed, which is related to transition into a different lithostratigraphic unit.

PCA was used to determine how radionuclide activities (^{238}U, ^{232}Th, ^{40}K) relate to specific mineral carriers and the physical properties of the sediments, namely Specific Surface Area (SSA) and the fine fraction (< 63 µm). When looking at the combined data (Fig. 7A and D), the PCA

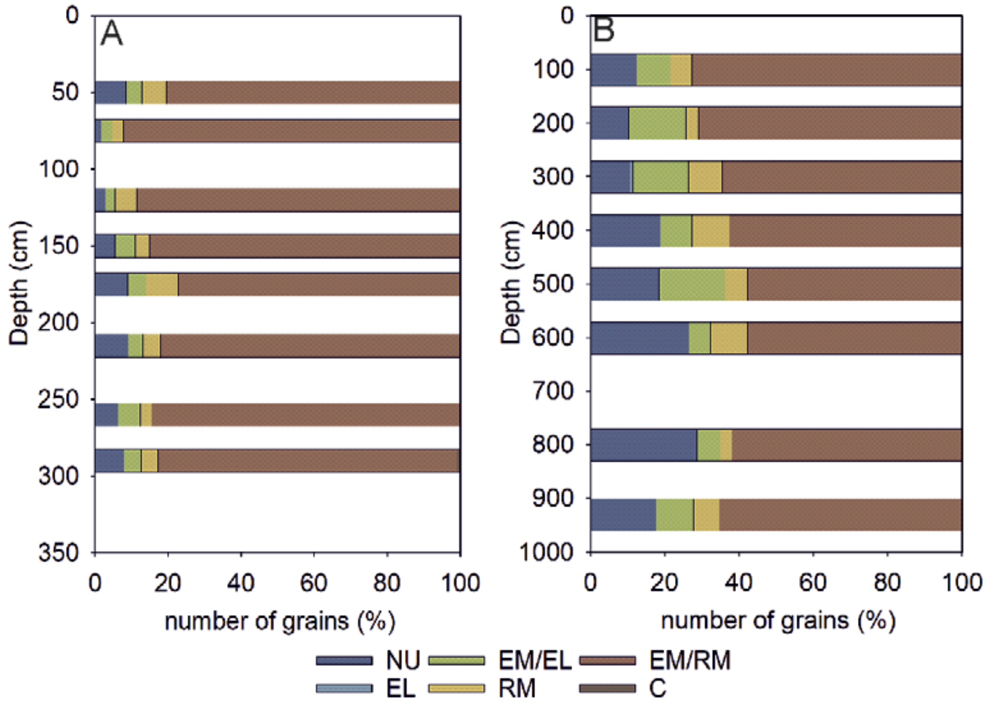

Fig. 5. Results of rounding and frosting analysis for the (A) Baranówko and (B) Kowalewo site.

clearly distinguishes two separate groups of sediments corresponding to the Baranówko and Kowalewo sites. These combined plots reveal a strong overall relationship between ^{238}U and ^{232}Th activities and the abundance of heavy minerals, as well as between ^{40}K activity and K-bearing minerals. When interpreted together with the QEMSCAN® data, these relationships indicate that zircon, rutile and ilmenite represent the principal mineral hosts associated with U and Th, whereas K-feldspar and fine-grained aluminosilicates are the principal hosts of ^{40}K. When interpreted together with the QEMSCAN® data, these relationships indicate that zircon, rutile and ilmenite represent the principal mineral hosts associated with U and Th. This relationship is further supported by our regression models (Figs. C2a and C2b in the Appendix). However, when we analyse the data separately for each site (Fig. 7B and C), these correlations become less distinct. This weaker relationship within individual profiles is primarily due to the very low variability of radionuclide activities within the uniform sedimentary layers. This suggests that local differences in the U and Th dose rates are driven largely by the sediment's mineralogical composition and physical properties. A completely different mechanism controls the distribution of ^{40}K. The PCA biplots show a close association between ^{40}K activity, the fine fraction and K-bearing minerals. QEMSCAN® identifies K-feldspar together with fine-grained aluminosilicates as the principal mineral hosts responsible for this relationship (Fig. 7D). However, on separate plots due to lack of changes in ^{40}K content, those correlations are virtually absent (Fig. 7E and F).

Kowalewo shows elevated content of heavy minerals and potassium-bearing minerals, which align with the higher ^{238}U, ^{232}Th, and ^{40}K activities observed in Kowalewo (Figs. 9D, D', E, E'). Conventional heavy-mineral analysis demonstrates that Kowalewo contains a higher proportion of heavy minerals than Baranówko. Interpreted together with the PCA results, this corresponds to the higher ^{238}U and ^{232}Th activities observed in Kowalewo. QEMSCAN® further identifies zircon, rutile, apatite and ilmenite as the principal mineral hosts associated with these radionuclides. However, distinction emerges between the two environments. QEMSCAN® identifies accessory heavy minerals that are interpreted as the principal hosts of U and Th. Based on the reduction in internal dose rate after HF treatment together with the QEMSCAN® mineralogical data, we infer independently that, radionuclide-bearing accessory mineral phases were preferentially associated with the outer parts of the density-separated quartz fraction in Kowalewo. In contrast, this effect is much less pronounced in Baranówko.. This distribution of U and Th between accessory mineral phases and grain-boundary coatings explains why the correlations between radionuclides and individual heavy minerals become less distinct when each site is analysed separately (Fig. 9C). In addition, less visible signal is also triggered by low ^{238}U, ^{232}Th content (see Figs. C2b and C2; Appendix).

Different mechanisms control the ^{40}K content. The PCA results for light and clay minerals (Fig. 9D) group ^{40}K directly with clay minerals, glauconite, and K-feldspar.

Aeolian maturity and multi-stage transport history

The quartz-grain surface characteristics and heavy-mineral assemblages provide consistent evidence for a domi-

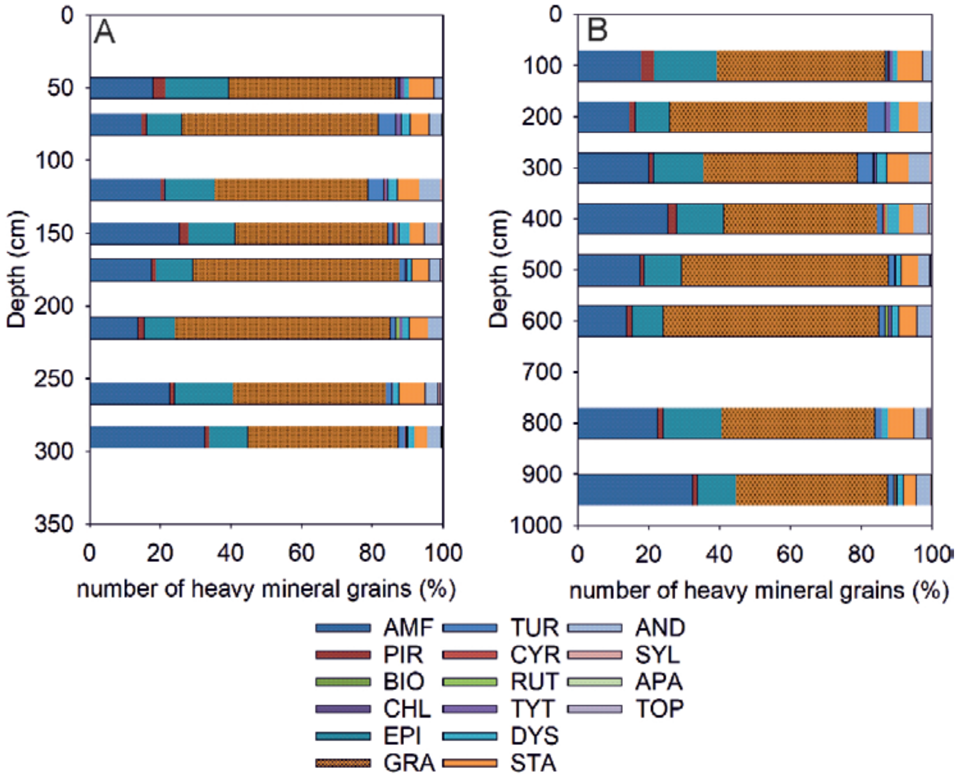

Fig. 6. Heavy mineral distribution for (A) Baranówko and (B) Kowalewo site.

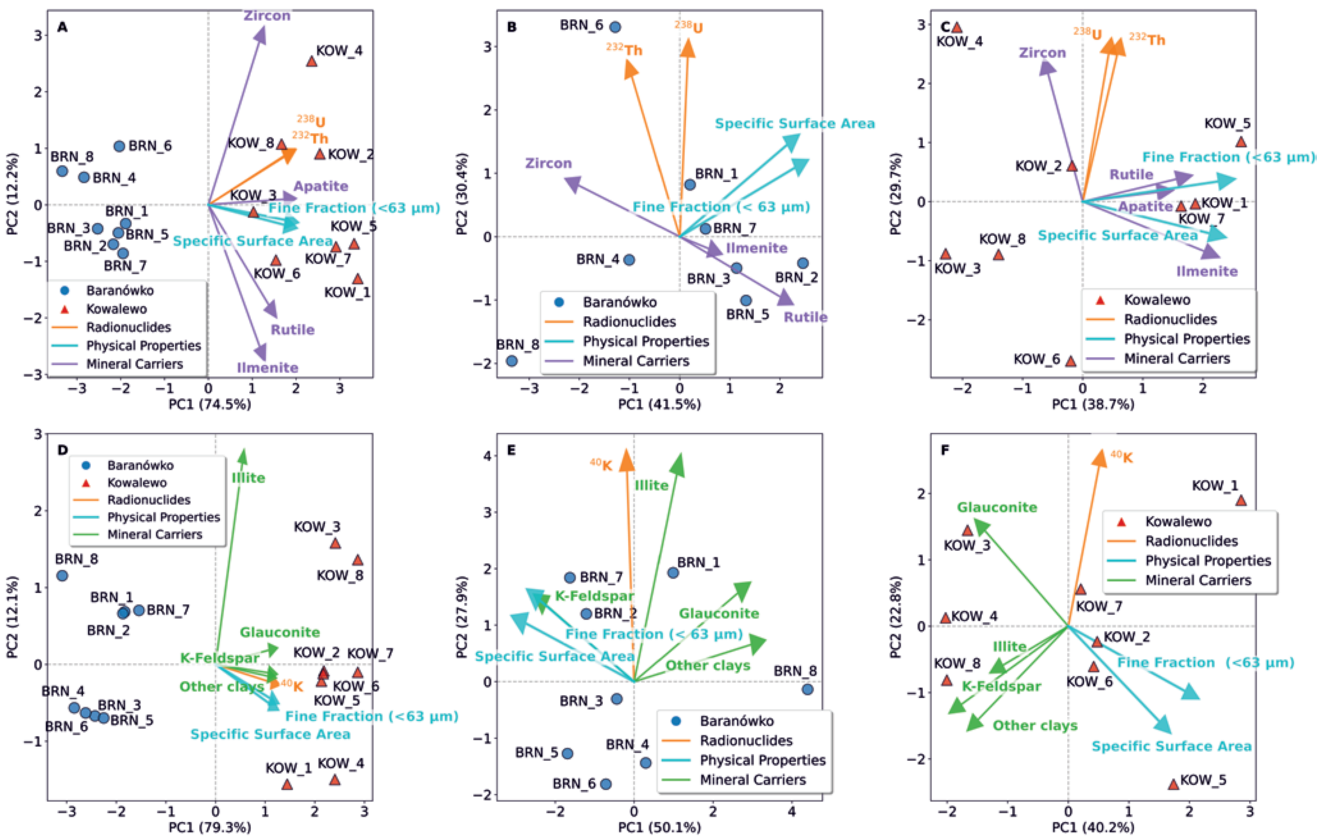

Fig. 7. PCA biplots illustrating the relationships between radionuclide activity concentrations, potential mineral carriers, and physical properties (Specific surface area and fine fraction <63 µm) of the analyzed sediments. The upper row displays the distribution and component loadings for heavy minerals alongside ^{238}U and ^{232}Th based on: (A) the combined dataset for both sites, (B) the Baranówko profile, and (C) the Kowalewo profile. The lower row presents an analogous analysis for light/clay minerals and ^{40}K for: (D) the combined dataset, (E) the Baranówko profile, and (F) the Kowalewo profile.

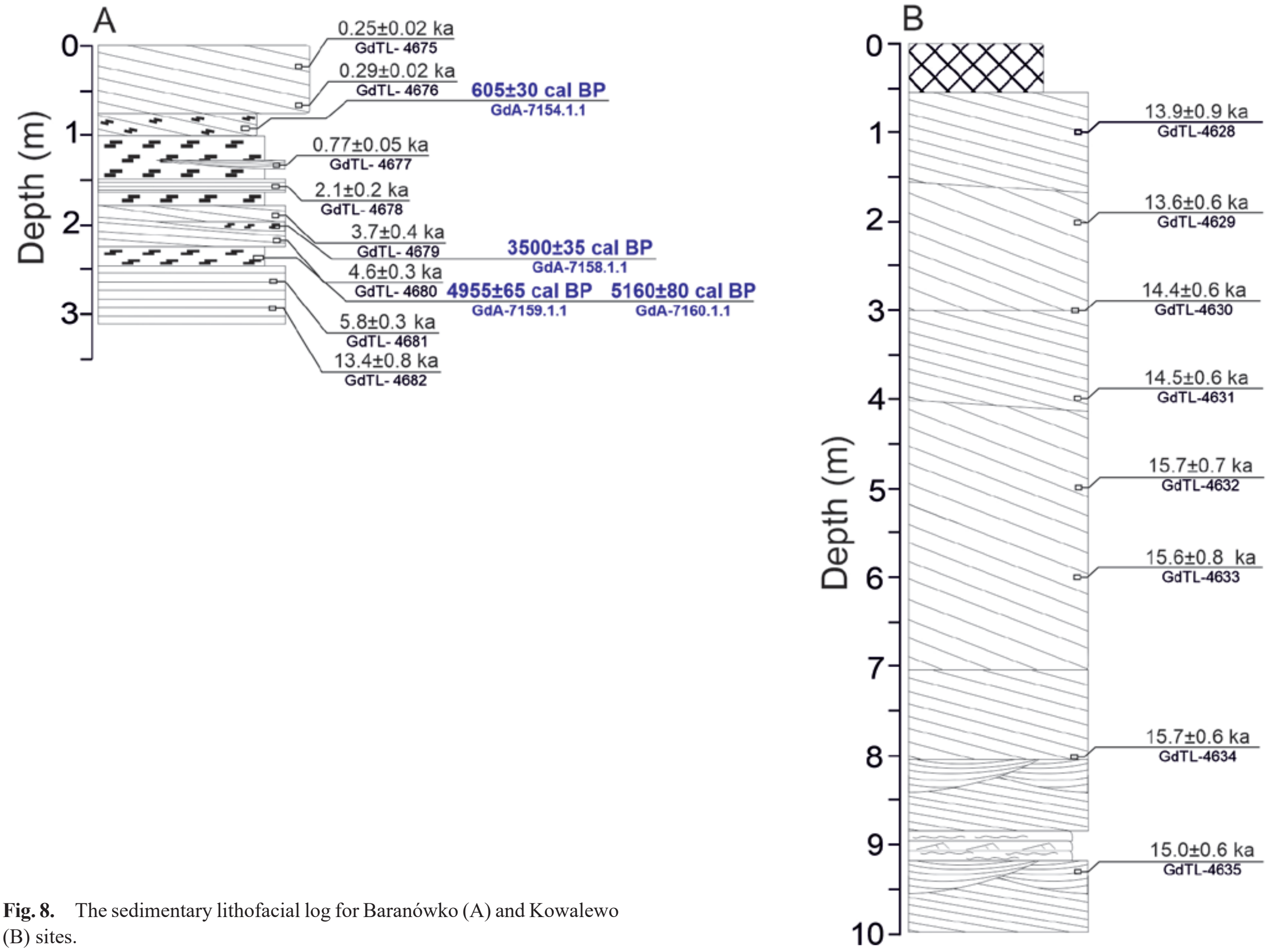

Fig. 8. The sedimentary lithofacial log for Baranówko (A) and Kowalewo (B) sites.

nant aeolian signal in both profiles, although with different degrees of sediment maturity and mixing. The quartz-grain analysis shows that both Baranówko and Kowalewo are dominated by the EM/RM class (Figs. 5A, B), indicating a strong aeolian overprint. This signal is more pronounced in Baranówko, where EM/RM grains usually exceed 77% and reach nearly 89% in BRN 3 (Fig. 5A), suggesting a more homogeneous and mature aeolian quartz-grain population. In Kowalewo, EM/RM grains are also dominant but occur in lower and more variable proportions, approximately 58–73%, together with higher shares of NU and EM/EL grains (Fig. 5B). This points to a greater admixture of fresh or less transformed material, probably related to fluvial or fluvio-aeolian input and a more complex depositional history.

The heavy-mineral data indicate that both profiles were supplied from broadly similar source material, as their assemblages are dominated by garnet, accompanied mainly by amphibole and epidote (Figs. 6A, B). However, Baranówko displays greater vertical variability in the proportions of these minerals (Figs. 6A), which may reflect local changes in sediment supply, sorting or reworking intensity. In contrast, Kowalewo shows a more uniform heavy-mineral composition, with consistently high garnet contents and subordinate amphibole and epidote (Fig. 6B). The absence of abrupt shifts in heavy-mineral composition suggests that no major change in sediment provenance occurred during deposition. Taken together, quartz-grain morphoscopy and conventional heavy-mineral analysis indicate that Baranówko records a more homogeneous and sedimentologically „old" aeolian succession, whereas Kowalewo preserves a more heterogeneous signature consistent with the contribution of fluvial or fluvio-aeolian material followed by aeolian reworking.

Despite the higher quartz-to-K-feldspar ratio in Baranówko than in Kowalewo (Figs. 9G, G'), the Baranówko material can be regarded as more ripe material in terms of the duration and intensity of sediment transport. The analysis of quartz-grain rounding and frosting indicates a predominance of moderately rounded and frosted grains (Fig. 7A). In the Baranówko profile (Fig. 8A), the heavy-mineral assemblage is dominated by garnets, which are considered among the most resistant minerals to mechanical abrasion. Binocular-microscope observations of garnet grains also indicate a relatively high degree of rounding and edge smoothing.

The predominance of moderately rounded and frosted quartz grains may indicate a relatively short episode of aeolian modification affecting grains that had already undergone earlier transport in a different sedimentary environment (Fig. 5A) (Mycielska-Dowigałło and Woronko, 1998). Previous studies on the provenance of sandy material in lowland valleys of the European Plain have shown that dune-building sands were commonly derived from fluvial

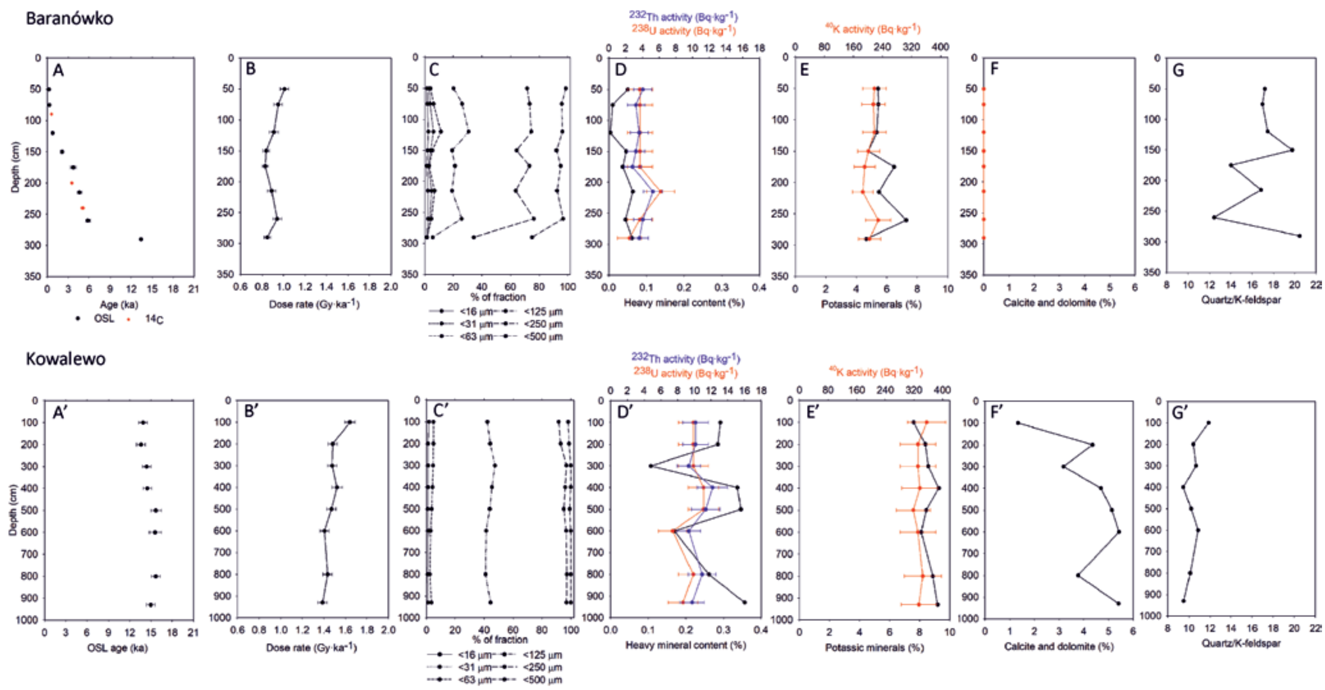

Fig. 9. Multi-proxy stratigraphic profiles for the studied sites. The plots illustrate depth-dependent variations in: (A, A') chronology, including OSL and ^{14}C ages; (B, B') total environmental dose rates; (C, C') grain size distribution; (D, D') heavy mineral content alongside ^{238}U and ^{232}Th activity concentrations; (E, E') potassium-bearing minerals compared with ^{40}K activity; (F, F') calcite and dolomite content; and (G, G') quartz/K-feldspar content. Plots designated with unprimed letters (A–G) correspond to the Baranówko profile, while plots with primed letters (A'–G') correspond to the Kowalewo profile.

deposits exposed during low-water stages and subsequently reworked by wind (Manikowska, 1995; Nowaczyk, 1986, 2000; Kasse, 1997, 2002; Zeeberg, 1998; Andrzejewski and Weckwerth, 2010; Vandenberghe *et al.*, 2013; Rychel *et al.*, 2018; Moska *et al.*, 2022; Łopuch and Jary, 2023). Thus, although the aeolisation of quartz grains may have been relatively short, the overall transport history of the grains was longer, with water acting as the primary transport medium and wind as the secondary reworking agent.

A similar interpretation can be proposed for the Kowalewo profile, although the sedimentary context is different. The Kowalewo material contains a lower proportion of K-feldspar than the Baranówko material (Fig. 9G'), while the analysis of quartz-grain rounding and frosting, as in Baranówko, shows a predominance of frosted grains (Fig. 5B). This suggests that the sediment was also affected by a two-stage transport history.

The higher degree of frosting and rounding of quartz grains, together with the greater proportion of garnets in the heavy-mineral assemblage, suggests that the Baranówko material experienced longer transport before accumulation than the Kowalewo material. Kowalewo profile developed on glacial and glaciofluvial sands (Włodek, 2004). This interpretation is supported by the presence of NU-type quartz grains, i.e. fresh, unmodified grains, which are commonly associated with glaciofluvial transport. Therefore, the Kowalewo sediments probably show shorter transport episodes, involving glaciofluvial supply, local fluvial or glaciofluvial reworking, and subsequent aeolian transformation.

The contrasts in mineralogical maturity between the two profiles are particularly visible in the carbonate content (Fig. 9F, F') and the heavy mineral ratios (Fig. 9D, D'). The calcite and dolomite content in Kowalewo are notably high, reaching 8–10%, whereas in Baranówko, these minerals are practically absent (Fig. 9F, F'). This lack of carbonates in Baranówko results from advanced secondary chemical weathering and prolonged decalcification (leaching) within a stable dune profile. The Śrem Basin itself, within which the Baranówko profile is located, represents an inherited geomorphological form that had previously been occupied and reworked by palaeoriver systems flowing through this area (Pawłowska *et al.*, 2022). Therefore, the material incorporated into the Baranówko dune may have undergone partial redeposition and assimilation from older fluvial deposits. This suggests that at least part of the sediment experienced a longer, multi-stage transport history before its final aeolian deposition. Furthermore, the quartz-to-K-feldspar ratio is higher in Baranówko than in Kowalewo (Fig. 9G, G'). This reflects the preferential removal of mechanically and chemically less stable feldspars during prolonged aeolian reworking and weathering in the Baranówko succession.

Chronology and phases of aeolian activity

The OSL ages for samples from the Kowalewo profile (13.6–15.7 ka) show limited variability across a broad range of sampling depths (100–930 cm), indicating a generally homogeneous depositional age of the sediments despite substantial variation in depth (Table A6b, Appendix). This suggests relatively rapid sediment accumulation under stable depositional conditions, most likely representing a single major phase of sedimentation with limited post-depositional disturbance.

In contrast, the OSL ages (0.25–13.4 ka) obtained from the Baranówko site (Table A6a; Appendix), distributed across depths of 50–290 cm, reveal a highly variable and non-linear age–depth relationship, indicating a complex depositional history. The observed variability likely reflects multiple phases of sediment accumulation interrupted by episodes of erosion, redeposition, or non-deposition, suggesting dynamic environmental conditions and significant post-depositional reworking of the sediments.

Both profiles analysed here represent a record of aeolian sedimentation, although they differ in sequence structure and in the chronology of aeolian activity. The Kowalewo profile (Fig. 8B) consists of two main units. The lower part of the profile is formed by fluvio-aeolian deposits, comprising fine sands with an intercalation showing ripple cross-lamination (Table D2a and D2b; Appendix), dated by OSL to 15.0 ± 0.6 ka (GdTL-4635). Deposition of these sediments preceded the main phase of dune sedimentation. The upper unit, composed of medium sands with tabular cross-stratification (Table D2a and D2b; Appendix), records continuous deposition of dune sands spanning the late Bølling and the entire Allerød, up to the onset of the Younger Dryas, between 15.7 ± 0.8 ka (GdTL-4633) and 13.9 ± 0.6 ka (GdTL-4628).

In the Baranówko profile (Fig. 8A), sedimentation begins with coarse sands showing laminar stratification (Table D1a and D1b; Appendix), dated to 13.4 ± 0.8 ka (GdTL-4682), indicating a phase of aeolian activity during the later part of the Bølling–Allerød interstadial. Four main soil horizons containing charcoal were identified within the profile and radiocarbon dated to 603.5 ± 52 cal BP (GdA-7154.1.1), 3505 ± 60 cal BP (GdA-7158.1.1), 4955 ± 90 cal BP (GdA-7159.1.1), and 5140 ± 155 cal BP (GdA-7159.1.1), (Table B1; Appendix). The soil–aeolian sequence consists mainly of medium sands with laminar stratification, separated by paleosoils horizons, and documents three main cycles of aeolian reactivation. The first cycle occurred during the Middle Holocene (GdTL-4681: 5.8 ± 1.0 ka; GdTL-4680: 4.6 ± 0.3 ka), the second during the Late Holocene (GdTL-4679: 3.7 ± 0.4 ka; GdTL-4678: 2.1 ± 0.2 ka), whereas the third represents the youngest, historical to modern phase of aeolian reactivation (GdTL-4677: 0.77 ± 0.05 ka; GdTL-4676: 0.29 ± 0.02 ka; GdTL-4675: 0.25 ± 0.02 ka).

CONCLUSION

Our multi-proxy evaluation of the Kowalewo and Baranówko profiles provides fundamental insights into the dynamics of environmental dose rates, leading to several essential conclusions for OSL dating:

1. Sediment type and radionuclide distribution. We demonstrate that sedimentary history, including transport intensity and the duration of chemical weathering, exerts a fundamental control on the distribution of radionuclide carriers. Consequently, reconstruction of the depositional environment is as important for reliable OSL dose rate assessment as the analytical precision of laboratory measurements.

2. Quartz-associated radionuclides and the internal dose component. In the Kowalewo profile, HF etching substantially reduced radionuclide activity in quartz separates, indicating that part of the uranium and thorium inventory was associated with grain surfaces or residual non-quartz phases rather than structurally incorporated within quartz. In contrast, this effect was negligible in the more texturally mature Baranówko sediments, suggesting limited surface-associated radionuclide accumulation. Although these observations provide important insight into the microdosimetric distribution of radionuclides, the resulting internal quartz dose represents only a minor contribution to the total environmental dose rate in both investigated profiles.

3. Controls on potassium distribution. QEMSCAN® indicates that potassium radioactivity is primarily associated with K-feldspar and fine-grained aluminosilicate. Although K-feldspar contributes substantially to the ^{40}K inventory, correlations within individual profiles indicate that additional potassium-bearing phases also influence the total potassium budget.

4. Crucial implications for OSL sampling and analysis. Our results demonstrate that ^{238}U, ^{232}Th and ^{40}K occur in a range of mineral hosts and sediment fractions whose distribution is controlled by sediment type and depositional history. For high-precision dating applications, this variability introduces severe micro-dosimetric complexities regarding not only the internal dose rate but also demand models that go beyond uniform radionuclide distribution (Cunningham and Wallinga, 2012).

5. Integration of complementary proxies. The complementary application of dosimetric methods, QEMSCAN® mineralogy, conventional heavy-mineral analysis and quartz-grain morphoscopy provides a more comprehensive framework for understanding radionuclide distribution than any individual method alone, thereby improving the robustness of environmental dose-rate assessment for OSL dating.

Acknowledgements

The presented results were obtained with the support of the Polish National Science Centre, contract number: 2021/41/N/ST10/00169.

REFERENCES

Aitken, M.J., 1985. Thermoluminescence Dating. London, Academic Press, 359.

Andrzejewski, L., Weckwerth, P., 2010. Dunes of the Toruń Basin against palaeogeographical conditions of the Late Glacial and Holocene. Ecological Questions 12, 9–15.

Antczak-Górka, B., 1995. Disappearance of the Warta River bifurcation in the Southern section of the Poznan gap during the Late Vistulian. Quaestiones Geographicae. Special Issue 4, 21–25.

Autzen, M., Andersen, C.E., Bailey, M., Murray, A.S., 2022. Calibration quartz: An update on dose calculations for luminescence dating. Radiation Measurements 157. https://doi.org/10.1016/j.radmeas.2022.106828.

Bell, W.T., 1979. Attenuation Factors for the Absorbed Radiation Dose in Quartz Inclusions for Thermoluminescence Dating. Ancient TL 8, 2–13.

Bohncke, S., Kasse, C., Vanderberghe, J., 1995. Climate induced environmental changes during the Vistulian Lateglacial at Żabinko, Poland. Questiones Geographicae, Special Issue 4, 43–64.

Bøtter-Jensen, L., Mejdahl, V., 1988. Assessment of beta dose-rate using a GM multicounter system. International Journal of Radiation Applications and Instrumentation. Part D. Nuclear Tracks and Radiation Measurements 14(1–2), 187–191. https://doi.org/10.1016/1359-0189(88)90062-3.

Brennan, B.J., Lyons, R., Phillips, S.W., 1991. Attenuation of alpha particle track dose for spherical grains. International Journal of Radiation Applications and Instrumentation. Part D. Nuclear Tracks and Radiation Measurements 18(1–2), 249–253. https://doi.org/10.1016/1359-0189(91)90119-3.

Brennan, B.J., 2003. Beta doses to spherical grains. Radiation Measurements 37(4–5), 299–303. https://doi.org/10.1016/S1350-4487(03)00011-8.

Bronk Ramsey, C., 2009. Bayesian analysis of radiocarbon dates. Radiocarbon 51, 337–360.

Cailleux, A., 1942. Les actions éoliennes périglaciaires en Europe. Mémoires de la Société Géologique de France, 41, 1–176.

Cunningham, A.C., Wallinga, J., 2012. Realizing the potential of fluvial archives using robust OSL chronologies. Quaternary Geochronology 12, 98–106. https://doi.org/10.1016/j.quageo.2012.05.007.

Folk, R.L., Ward, W.C., 1957. Brazos River bar: A study in the significance of grain size parameters. Journal of Sedimentary Petrology 27(1), 3–26. https://doi.org/10.1306/74D70646-2B21-11D7-8648000102C1865D.

Galbraith, R.F., Roberts, R.G., Laslett, G.M., Yoshida, H., Olley, J.M., 1999. Optical dating of single and multiple grains of quartz from Jinminum Rock Shelter, Northern 12 Australia. Part I,experimental design and statistical models. Archaeometry 41, 1835–1857.

Gonera, P., Kozarski, S., 1987. River channel changes and rough paleodischarge estimates for the Warta River, west-central Poland. Geografiska Annaler: Series A, Physical Geography 69(1), 163–171.

Guérin, G., Mercier, N., Adamiec, G., 2011. Dose-rate conversion factors: update. Ancient TL 29, 5-8.

Kasse, C., 1997. Cold-Climate Aeolian Sand–Sheet Formation in North–Western Europe (c. 14–12.4 ka); a response to Permafrost Degradation and Increased Aridity. Permafrost and Periglacial Processes 8, 295–311. https://doi.org/10.1002/(SICI)1099-1530(199709)8:3<295::AID-PPP256>3.0.CO;2-0.

Kasse, C., 2002. Sandy aeolian deposits and their relation to climate during the Last Glacial Maximum and Lateglacial in northwest and central Europe. Progress in Physical Geography 26, 507–532. https://doi.org/10.1191/0309133302pp350ra.

Kenis, P., Skurzyński, J., Jary, Z., Kubik, R., 2020. A new methodological approach (QEMSCAN®) in the mineralogical study of Polish loess: Guidelines for further research. Open Geosciences 12(1), 342-353.

Kenis, P., Skurzyński, J., Arabasz, S., Jary, Z., 2025. Beyond the limitations of bulk sample geochemistry: extended paleoenvironmental interpretation of the Late Pleistocene loess-paleosol sequence at Tyszowce (SE Poland) based on automated whole-rock mineralogical analysis (QEMSCAN®) and single grain SEM-EDS investigation. Catena 249, 108704. https://doi.org/10.1016/j.catena.2025.108704

Kolb, T., Tudyka, K., Kadereit, A., Lomax, J., Poręba, G., Zander, A., Zipf, L., Fuchs, M., 2022. The µDOSE system: determination of environmental dose rates by combined alpha and beta counting – performance tests and practical experiences. Geochronology 4, 1–31. https://doi.org/10.5194/gchron-4-1-2022.

Kozarski, S., 1988. Origin of pradolinas: a discussion of mistaken ideas. Zeitschrift für Gletscherkunde und Glazialgeologie 24, 75–92.

Kozarski, S., 1995. Deglacjacja północno-zachodniej Polski: warunki środowiska i transformacja geosystemu (20 ka > 10 ka BP). Dokumentacja Geograficzna 1, 1–82.

Kreutzer, S., Burow, C., Dietze, M., Fuchs, M., Schmidt, C., Fischer, M., Friedrich, J., Riedesel, S., Autzen, M., Mittelstrass, D., 2020. Luminescence: Comprehensive Luminescence Dating Data Analysis. R package version 0.9.10. Accessed July 28, 2021. https://CRAN.R-project.org/package=Luminescence.

Krinsley, D.H., Margolis, S.V., 1969. A study of quartz sand grain surface textures with the scanning electron microscope. Transactions of the New York Academy of Sciences, Series II 31, 457–477.

Krinsley, D.H., Doornkamp, J.C., 1973. Atlas of Quartz Sand Surface Textures. Cambridge University Press, Cambridge.

Łopuch, M., Jary Z., 2023. Sand sources and migration of the dune fields in the central European Sand Belt – A pattern analysis approach. Geomorphology 439, 108856. https://doi.org/10.1016/j.geomorph.2023.108856.

Mahaney, W.C., 2002. Atlas of Sand Grain Surface Textures and Applications. Oxford University Press, Oxford/New York, 237.

Mange, M.A., Maurer, F.W., 1992. Heavy Minerals in Colour. Chapman & Hall, London,1–147. https://doi.org/10.1007/978-94011-2308-2.

Manikowska, B., 1995. Aeolian activity differentiation in the area of Poland during the period 20–8 ka BP. Biuletyn Peryglacjalny 34, 125–165.

Marks, L., Bitinas, A., Blaszkiewicz, M., Borner, A., Guobyte, R., Rinterknecht, V., Tylmann, K., 2022. Glacial landscapes of Northern Central Europe. In: Palacios, D., Hughes, P.D., García-Ruiz, J.M., Andr´es, N. (Eds), European Glacial Landscapes. Maximum Extent of Glaciations. Elsevier, Amsterdam, 45–52. https://doi.org/10.1016/B978-0-12-823498-3.00007-8.

Marks, L., Bitinas, A., Blaszkiewicz, M., Borner, A., Guobyte, R., Rinterknecht, V., Tylmann, K., 2023. Chapter 11: Northern Central Europe: glacial landforms during deglaciation (18.9–14.9 ka). In: Palacios, D., Hughes, P.D., García-Ruiz, J.M., Andr´es, N. (Eds), European Glacial Landscapes. The Last Deglaciation. Elsevier, Amsterdam, 95–104. https://doi.org/10.1016/B978-0-323-91899-2.00008-5.

Mason, J.A., Jacobs, P.M., Greene, R.S.B., 2003. Sedimentary aggregates in the Peoria Loess of Nebraska, USA. Catena 53, 377–397. https://doi.org/10.1016/S0341-8162(03)00073-0.

Moska, P., 2019. Luminescence dating of Quaternary sediments – some practical aspects. Studia Quaternaria 36(2), 161–169.

Moska, P., Sokołowski, R.J., Jary, Z., Zieliński, P., Raczyk, J., Szymak, A., Krawczyk, M., Skurzyński, J., Poręba, G., Łopuch, M., Tudyka, K., 2022. Stratigraphy of the Late Glacial and Holocene aeolian series in different sedimentary zones related to the Last Glacial maximum in Poland. Quaternary International 630, 65–83. https://doi.org/10.1016/j.quaint.2021.04.004.

Murray, A.S., Wintle, A.G., 2000. Luminescence dating of quartz using an improved single aliquot regenerative-dose protocol. Radiation Measurements 32, 57–73.

Murray, A.S., Helsted, L.M., Autzen, M., Jain, M., Buylaert, J.P., 2018. Measurement of natural radioactivity: Calibration and performance of a high-resolution gamma spectrometry facility. Radiation Measurements 120, 215-220. https://doi.org/10.1016/j.radmeas.2018.04.006.

Mycielska-Dowgiałło, E., Woronko, B., 1998. Analiza obtoczenia i zmatowienia ziarn kwarcowych frakcji piaszczystej i jej wartość interpretacyjna. Przegląd Geologiczny 46(12), 1275-1281.

Nowaczyk, B., 1986. Wiek wydm, ich cechy granulometryczne i strukturalne a schemat cyrkulacji atmosferycznej w Polsce w późnym vistulianie i holocenie [The age of dunes, their textural and structural properties against atmospheric circulation pattern of Poland during the Late Vistulian and Holocene]. Wydawnictwo Naukowe UAM, 245.

Nowaczyk, B., 2000. Development of dunes and eolian cover sands in Poland in the Late Vistulian and Holocene. In: Chojnicki, Z., Parysek, J.J. (Eds.), Polish Geography: Problems, Researches, Applications. Bogucki Wydawnictwo Naukowe, Poznań, 133–151.

Nowak, J., 2001. Szczegółowa Mapa Geologiczna Polski w skali 1:50 000, Ark. Śrem [Detailed Geological Map of Poland, 1:50000, sheet Śrem]. Polish Geological Institute, Warsaw (in Polish).

Pawłowska, K., Zieliński, T., Woronko, B., Sobkowiak-Tabaka, I., Stachowicz-Rybka, R., 2022. Integrated environmental records in Late Pleistocene Poland: The paleofluvial regime and paleoclimate inferred from Krosinko site. Quaternary International 616, 12–29.

Pirrie, D., Rollinson, G.K., 2011. Unlocking the applications of automated mineral analysis. Geology Today 27(6), 226-235.

Pisarska-Jamroży, M., 2015. Factors controlling sedimentation in the Toruń–Eberswalde ice-marginal valley during the Pomeranian phase of the Weichselian glaciation: an overview. Geologos 21(1), 1–29. https://doi.org/10.1515/logos-2015-0001.

Poręba, G., Tudyka, K., Walencik-Łata, A., Kolarczyk, A., 2020. Bias in ^{238}U decay chain members measured by γ-ray spectrometry due to ^{222}Rn leakage. Applied Radiation and Isotopes 156. https://doi.org/10.1016/j.apradiso.2019.108945.

Poręba, G., Tudyka, K., Szymak, A., Pluta, J., Rocznik, J., Świątkowski, J., Osadnik, R., Moska, P., 2022. Evaluating the effect of hydrofluoric acid etching on quartz grains using microscope image analysis, laser diffraction and weight loss particle size estimate, Geochronometria 49. https://doi.org/10.2478/geochr-2022-0001.

Prescott, J.R., Hutton, J.T., 1994. Cosmic ray contributions to dose rates for luminescence and ESR dating, large depths and long-term variations. Radiation Measurements 23, 497-500. https://doi.org/10.1016/1350-4487(94)90086-8.

Reed, S.J.B., 2005. Electron microprobe analysis and scanning electron microscopy in geology. Cambridge University Press.

Reimer, P., Austin, W., Bard, E., Bayliss, A., Blackwell, P., Bronk Ramsey, C., Butzin, M., Cheng, H., Edwards, R., Friedrich, M., Grootes, P., Guilderson, T., Hajdas, I., Heaton, T., Hogg, A., Hughen, K., Kromer, B., Manning, S., Muscheler, R., Palmer, J., Pearson, C., van der Plicht, J., Reimer, R., Richards, D., Scott, E., Southon, J., Turney, C., Wacker, L., Adolphi, F., Büntgen, U., Capano, M., Fahrni, S., Fogtmann-Schulz, A., Friedrich, R., Köhler, P., Kudsk, S., Miyake, F., Olsen, J., Reinig, F., Sakamoto, M., Sookdeo, A., Talamo, S., 2020. The IntCal20 Northern Hemisphere radiocarbon age calibration curve (0–55 cal kBP). Radiocarbon 62, 725–757.

Rychel, J., Woronko, B., Błaszkiewicz, M., Karasiewicz, T., 2018. Aeolian processes records within the last glacial limit areas based on the Płock basin case (Central Poland). Bulletin of the Geological Society of Finland 90(2), 55–69. https://doi.org/10.17741/bgsf/90.2.007.

Sanderson, D.C.W., 1988, Thick source beta counting (TSBC): A rapid method for measuring beta dose-rates. International Journal of Radiation Applications and Instrumentation. Part D. Nuclear Tracks and Radiation Measurements 14(1–2), 203–207. https://doi.org/10.1016/1359-0189(88)90065-9.

Severin, K.P., 2004. Energy dispersive spectrometry of common rock forming minerals. Dordrecht, The Netherlands: Kluwer Academic.

Schulz, B., Sandmann, D., and Gilbricht, S., 2020. SEM-Based Automated Mineralogy and Its Application in Geo- and Material Sciences. Minerals 10(11), 1004. https://doi.org/10.3390/min10111004.

Solon, J., Borzyszkowski, J., Bidłasik ,M., Richling, A., Badora, K., Balon, J., Brzezińska-Wójcik, T., Chabudziński, Ł., Dobrowolski, R., Grzegorczyk, I., Jodłowski, M., Kistowski, M., Kot, R., Krąż, P., Lechnio, J.R., Macias, A., Majchrowska, A., Malinowska, E., Migoń, P., Myga-Piątek, U., Nita, J., Papińska, E., Rodzik, J., Strzyż, M., Terpiłowski, S., Ziaja, W., 2018. Physico-geographical mesoregions of Poland: Verification and adjustment of boundaries on the basis of contemporary spatial data. Geographia Polonica 91(2), 143-170. https://doi.org/10.7163/GPol.0115.

Synal, H.-A., Stocker, M., Suter, M., 2007. *MICADAS:* A new compact radiocarbon AMS system. Nuclear Instruments and Methods in Physics Research Section B: Beam Interactions with Materials and Atoms 259(1), 7–13. https://doi.org/10.1016/j.nimb.2007.01.138.

Szymak, A., Moska, P., Poręba, G., Tudyka, K., Adamiec, G., 2022. The internal dose rate in quartz grains: experimental data and consequences for luminescence dating. Geochronometria 49. https://doi.org/10.2478/geochr-2022-0002.

Szymak, A., Moska, P., Sokołowski, R.J., Poręba, G., Tudyka, K., 2024. Chronostratigraphy of the Late Glacial Żabinko site (Western Poland) and investigation of the dose rate variability. Geochronometria 51, 189750. https://doi.org/ https://doi.org/10.20858/geochr/189750.

Thompson, M., Ellison, S.L.R., Wood, R., 2002. Harmonized guidelines for single-laboratory validation of methods of analysis (IUPAC Technical Report). Pure and Applied Chemistry 74(5), 835-855. https://doi.org/ https://doi.org/10.1351/pac200274050835.

Tudyka, K., Miłosz, S., Adamiec, G., Bluszcz,. A, Poręba, G., Paszkowski, Ł., Kolarczyk, A., 2018. µDOSE: A compact system for environmental radioactivity and dose rate measurement. Radiation Measurement 118, 8-13. https://doi.org/10.1016/J.RADMEAS.2018.07.016.

Tudyka, K., Bluszcz, A., Poręba, G., Miłosz, S., Adamiec, G., Kolarczyk, A., Kolb, T., Lomax, J., Fuchs, M., 2020. Increased dose rate precision in combined α and β counting in the µDose system – a probabilistic approach to data analysis. Radiation Measurements 134, 106310. https://doi.org/10.1016/j.radmeas.2020.106310.

Tudyka, K., Poręba, G., Szymak, A., Rocznik, J., Pluta, J., Schüler, T., Kolb, T., Murray, A., 2021. Systematic error in ^{238}U decay chain radionuclides measurements due to ^{222}Rn emanation from reference materials. Measurement 184, 109893. https://doi.org/10.1016/j.measurement.2021.109893.

Tudyka, K., Koruszowic, M., Osadnik, R., Adamiec, G., Moska, P., Szymak, A., Bluszcz, A., Zhang, J., Kolb, T., Poręba, G., 2022. µRate: An online dose rate calculator for trapped charge dating. Archaeometry 65, 423-443. https://doi.org/10.1111/arcm.12828.

Włodek, M., 2002. Szczegółowa Mapa Geologiczna Polski w skali 1:50 000, Ark. Żnin [Detailed Geological Map of Poland, 1:50000, sheet Żnin]. Polish Geological Institute, Warsaw (in Polish).

Włodek, M., 2004. Objaśnienia do Szczegółowej Mapy Geologicznej Polski w skali 1:50 000, Ark. Żnin [Explanation of the Detailed Geological Map of Poland, 1:50000, sheet Żnin]. Polish Geological Institute, Warsaw (in Polish).

Wysota, W., Molewski, P., Sokołowski, R., 2009. Record of the Vistula ice lobe advances in the Late Weichselian glacial sequence in north-central Poland. Quaternary International 207, 26–41. https://doi.org/10.1016/j.quaint.2008.12.015.

Vandenberghe, D.A.G., Derese, C., Kasse, C., Van den Haute, P., 2013. Late Weichselian (fluvio-) aeolian sediments and Holocene drift-sands of the classic type locality in Twente (E Netherlands): a high-resolution dating study using optically stimulated luminescence. Quaternary Science Reviews 68, 96–113. https://doi.org/0.1016/j.quascirev.2013.02.009.

Zeeberg, J., 1998. The European sand belt in eastern Europe and comparison of Late Glacial dune orientation with GCM simulation results. Boreas 27, 127–139. https://doi.org/10.1111/j.1502-3885.1998.tb00873. x.

Zieliński, P., Issmer, K., 2008. Propozycja kodu genetycznego osadów środowiska eolicznego. (The proposal of genetic code of aeolian deposits). Przegląd Geologiczny 56, 67–72 (in Polish).

Zieliński, P., Sokołowski, R.J., Fedorowicz, S., Jankowski, M., 2011. Stratigraphic position of fluvial and aeolian deposits in the Żabinko site based on TL dating. Geochronometria 38, 64–71. https://doi.org/10.2478/s13386-011-0005-x.

APPENDIX

Section A: OSL dating results

Table A1a. Equivalent dose for Baranówko site.

Lab. Code	Sample ID	Equivalent dose (Gy)
GdTL_4675	Baranówko_1	0.32±0.02
GdTL_4676	Baranówko _2	0.34±0.01
GdTL_4677	Baranówko _3	0.75±0.02
GdTL_4678	Baranówko _4	1.8±0.2
GdTL_4679	Baranówko _5	3.0±0.3
GdTL_4680	Baranówko _6	4.1±0.2
GdTL_4681	Baranówko _7	5.3±0.1
GdTL_4682	Baranówko _8	10.7±0.3

Table A1b. Equivalent dose for Kowalewo site.

Lab. Code	Sample ID	Equivalent dose (Gy)
GdTL_4628	Kowalewo_1	23.4±0.7
GdTL_4629	Kowalewo _2	20.4±0.5
GdTL_4630	Kowalewo _3	22.8±0.5
GdTL_4631	Kowalewo _4	22.8±0.5
GdTL_4632	Kowalewo _5	23.9±0.7
GdTL_4633	Kowalewo _6	22.1±0.8
GdTL_4634	Kowalewo _7	22.6±0.5
GdTL_4635	Kowalewo _8	21.3±0.6

Table A2a. HPGe high-resolution spectrometry radionuclide activities from the ^{238}U, ^{232}Th, ^{40}K for Baranówko. External dose rate includes cosmic rate.

Lab. Code	Sample ID	Sampling depth (cm)	Moisture content (%)	^{232}Th ($Bq \cdot kg^{-1}$)	^{238}U ($Bq \cdot kg^{-1}$)	^{40}K ($Bq \cdot kg^{-1}$)	External dose rate ($Gy \cdot ka^{-1}$)
GdTL_4675	Baranówko_1	50	15±5	3.9±0.4	3.4±0.3	229±18	0.95±0.05
GdTL_4676	Baranówko _2	75	15±5	4.8±0.4	4.2±0.4	242±19	1.00±0.06
GdTL_4677	Baranówko _3	120	15±5	3.7±0.4	3.8±0.4	227±17	0.92±0.05
GdTL_4678	Baranówko _4	150	15±5	3.3±0.3	3.0 ±0.3	235±18	0.92±0.05
GdTL_4679	Baranówko _5	175	15±5	3.6±0.4	3.7±0.4	215±17	0.87±0.05
GdTL_4680	Baranówko _6	215	15±5	4.6±0.4	4.9±0.4	201±16	0.86±0.05
GdTL_4681	Baranówko _7	260	15±5	5.0±0.4	5.4±0.4	241±19	0.98±0.06
GdTL_4682	Baranówko _8	290	15±5	4.2±0.3	3.7±0.3	215±16	0.86±0.05

Table A2b. HPGe high-resolution spectrometry radionuclide activities from the ^{238}U, ^{232}Th, ^{40}K for Kowalewo. External dose rate includes cosmic rate.

Lab. Code	Sample ID	Sampling depth (cm)	Moisture content (%)	^{232}Th ($Bq \cdot kg^{-1}$)	^{238}U ($Bq \cdot kg^{-1}$)	^{40}K ($Bq \cdot kg^{-1}$)	External dose rate ($Gy \cdot ka^{-1}$)
GdTL_4628	Kowalewo_1	100	7±3	10.5±0.5	11.5±0.5	360±27	1.64±0.08
GdTL_4629	Kowalewo _2	200	7±3	9.4±0.5	8.7±0.4	350±27	1.52±0.08
GdTL_4630	Kowalewo _3	300	7±3	9.2±0.5	10.2±0.5	370±28	1.58±0.08
GdTL_4631	Kowalewo _4	400	7±3	11.5±0.6	10.5±0.4	367±28	1.59±0.08
GdTL_4632	Kowalewo _5	500	7±3	11.9±0.5	11.9±0.5	353±27	1.57±0.08
GdTL_4633	Kowalewo _6	600	7±3	8.8±0.5	8.7±0.4	350±27	1.44±0.08
GdTL_4634	Kowalewo _7	800	7±3	9.3±0.4	9.8±0.4	368±28	1.50±0.08
GdTL_4635	Kowalewo _8	930	7±3	8.5±0.5	9.8±0.4	368±28	1.48±0.08

Table A3a. ICP-MS ^{238}U, ^{232}Th, ^{40}K converted to radionuclide activities for Baranówko. External dose rate includes cosmic rate.

Lab. Code	Sample ID	Sampling depth (cm)	Moisture content (%)	^{232}Th (Bq·kg^{-1})	^{238}U (Bq·kg^{-1})	^{40}K (Bq·kg^{-1})	External dose rate (Gy·ka^{-1})
GdTL_4675	Baranówko_1	50	15±5	4.1±1.1	3.7±1.5	217±33	0.93±0.08
GdTL_4676	Baranówko _2	75	15±5	3.3±1.0	3.7±1.5	215±32	0.89±0.08
GdTL_4677	Baranówko _3	120	15±5	3.7±1.1	3.7±1.5	217±33	0.89±0.08
GdTL_4678	Baranówko _4	150	15±5	3.3±1.0	3.7±1.5	201±30	0.84±0.08
GdTL_4679	Baranówko _5	175	15±5	2.8±1.0	3.7±1.5	191±29	0.79±0.07
GdTL_4680	Baranówko _6	215	15±5	5.3±1.1	6.2±1.6	186±28	0.85±0.07
GdTL_4681	Baranówko _7	260	15±5	4.1±1.1	3.7±1.5	228±34	0.90±0.08
GdTL_4682	Baranówko _8	290	15±5	3.7±1.1	2.5±1.4	204±31	0.80±0.07

Table A3b. ICP-MS ^{238}U, ^{232}Th, ^{40}K converted to radionuclide activities for Kowalewo. External dose rate includes cosmic rate.

Lab. Code	Sample ID	Sampling depth (cm)	Moisture content (%)	^{232}Th (Bq·kg^{-1})	^{238}U (Bq·kg^{-1})	^{40}K (Bq·kg^{-1})	External dose rate: (Gy·ka^{-1})
GdTL_4628	Kowalewo_1	100	7±3	10.2±1.5	9.9±1.8	355±53	1.59±0.14
GdTL_4629	Kowalewo _2	200	7±3	10.2±1.5	9.9±1.8	331±50	1.49±0.13
GdTL_4630	Kowalewo _3	300	7±3	9.3±1.4	9.9±1.8	331±50	1.46±0.13
GdTL_4631	Kowalewo _4	400	7±3	12.2±1.8	11.1±1.8	337±51	1.53±0.13
GdTL_4632	Kowalewo _5	500	7±3	11.4±1.7	11.1±1.8	318±48	1.44±0.12
GdTL_4633	Kowalewo _6	600	7±3	9.3±1.4	7.4±1.7	331±50	1.37±0.13
GdTL_4634	Kowalewo _7	800	7±3	11.0±1.6	9.9±1.8	345±52	1.46±0.13
GdTL_4635	Kowalewo _8	930	7±3	9.7±1.5	8.7±1.7	334±50	1.38±0.13

Table A4a. μDOSE system radionuclide activities from the ^{238}U, ^{232}Th, ^{40}K for Baranówko. External dose rate includes cosmic rate.

Lab. Code	Sample ID	Sampling depth (cm)	Moisture content (%)	^{232}Th (Bq·kg^{-1})	^{238}U (Bq·kg^{-1})	^{40}K (Bq·kg^{-1})	External dose rate (Gy·ka^{-1})
GdTL_4675	Baranówko_1	50	15±5	2.0±3.0	25.1±2.9	117±16	1.05±0.07
GdTL_4676	Baranówko _2	75	15±5	5.2±1.0	4.56±0.98	232±14	0.91±0.04
GdTL_4677	Baranówko _3	120	15±5	3.2±1.9	4.4±1.8	232±16	0.86±0.04
GdTL_4678	Baranówko _4	150	15±5	4.73±0.85	1.54±0.79	213±14	0.78±0.04
GdTL_4679	Baranówko _5	175	15±5	1.8±1.4	6.9±1.4	195±15	0.77±0.04
GdTL_4680	Baranówko _6	215	15±5	6.7±3.2	13.0±3.1	174±16	0.88±0.04
GdTL_4681	Baranówko _7	260	15±5	5.36±0.92	3.80±0.86	236±14	0.87±0.04
GdTL_4682	Baranówko _8	290	15±5	3.1±1.7	3.7±1.6	205±16	0.74±0.04

Table A4b. μDOSE system radionuclide activities from the ^{238}U, ^{232}Th, ^{40}K for Kowalewo. External dose rate includes cosmic rate.

Lab. Code	Sample ID	Sampling depth (cm)	Moisture content (%)	^{232}Th (Bq·kg^{-1})	^{238}U (Bq·kg^{-1})	^{40}K (Bq·kg^{-1})	External dose rate (Gy·ka^{-1})
GdTL_4628	Kowalewo_1	100	7±3	17.9±2.7	9.0±2.5	384±18	1.71±0.06
GdTL_4629	Kowalewo _2	200	7±3	10.1±1.4	11.4±1.4	340±16	1.47±0.05
GdTL_4630	Kowalewo _3	300	7±3	10.9±2.2	10.3±2.0	376±17	1.55±0.05
GdTL_4631	Kowalewo _4	400	7±3	12.1±2.4	12.5±2.2	360±17	1.54±0.05
GdTL_4632	Kowalewo _5	500	7±3	12.5±1.7	13.0±1.6	343±16	1.50±0.05
GdTL_4633	Kowalewo _6	600	7±3	14.1±1.9	8.3±1.8	339±17	1.42±0.05
GdTL_4634	Kowalewo _7	800	7±3	6.0±1.4	13.7±1.4	354±16	1.40±0.05
GdTL_4635	Kowalewo _8	930	7±3	10.3±1.9	9.2±1.8	357±17	1.39±0.05

Table A5a. Internal dose rates for Baranówko. Internal dose rate was calculated based on the weighted-mean radioactivity from ICP-MS, μDOSE.

Lab. Code	Sample ID	Internal dose rate (Gy·ka^{-1}) – μDOSE system				Internal dose rate (Gy·ka^{-1}) – ICP-MS		Internal dose rate (Gy·ka^{-1})
		After density separation		After HF		After density separation	After HF	After HF
		unmilled	milled	unmilled	milled	milled	milled	milled
GdTL_4675	Baranówko_1	0.018±0.009	0.021±0.010	0.000±0.011	0.011±0.010	0.028±0.017	0.020±0.016	0.0083±0.0083
GdTL_4676	Baranówko _2	0.005±0.005	0.010±0.007	0.003±0.010	0.014±0.009	0.029±0.017	0.020±0.016	0.0075±0.0075
GdTL_4677	Baranówko _3	0.007±0.005	0.014±0.007	0.006±0.009	0.022±0.010	0.027±0.017	0.020±0.016	0.0088±0.0075
GdTL_4678	Baranówko _4	0.007±0.005	0.027±0.013	0.006±0.010	0.020±0.011	0.027±0.017	0.023±0.017	0.0108±0.089
GdTL_4679	Baranówko _5	0.011±0.007	0.022±0.009	0.001±0.010	0.020±0.009	0.028±0.017	0.020±0.016	0.0075±0.0071
GdTL_4680	Baranówko _6	0.004±0.006	0.013±0.008	0.009±0.009	0.023±0.017	0.029±0.017	0.023±0.017	0.018±0.013
GdTL_4681	Baranówko _7	0.006±0.005	0.007±0.005	0.011±0.010	0.024±0.010	0.029±0.017	0.020±0.016	0.0100±0.083
GdTL_4682	Baranówko _8	0.010±0.006	0.012±0.007	0.011±0.010	0.024±0.010	0.028±0.017	0.020±0.016	0.0104±0.086

Table A5b. Internal dose rates for Kowalewo. Internal dose rate was calculated based on the weighted-mean radioactivity from ICP-MS, μDOSE.

Lab. Code	Sample ID	Internal dose rate (Gy·ka^{-1}) – μDOSE system				Internal dose rate (Gy·ka^{-1}) – ICP-MS		Internal dose rate (Gy·ka^{-1})
		After density separation		After HF		After density separation	After HF	After HF
		unmilled	milled	unmilled	milled	milled	milled	milled
GdTL_4628	Kowalewo_1	0.023±0.008	0.028±0.008	0.025±0.011	0.017±0.011	0.045±0.023	0.009±0.073	0.0064±0.0056
GdTL_4629	Kowalewo _2	0.033±0.011	0.037±0.012	0.020±0.010	0.008±0.010	0.049±0.024	0.012±0.084	0.0072±0.0058
GdTL_4630	Kowalewo _3	0.027±0.010	0.037±0.013	0.022±0.009	0.017±0.009	0.049±0.024	0.009±0.073	0.0165±0.0094
GdTL_4631	Kowalewo _4	0.033±0.012	0.032±0.011	0.018±0.011	0.016±0.010	0.052±0.024	0.009±0.073	0.0060±0.0053
GdTL_4632	Kowalewo _5	0.032±0.014	0.030±0.010	0.005±0.010	0.000±0.009	0.049±0.024	0.009±0.073	0.0048±0.0051
GdTL_4633	Kowalewo _6	0.023±0.008	0.040±0.012	0.009±0.009	0.000±0.009	0.048±0.023	0.009±0.073	0.0046±0.0050
GdTL_4634	Kowalewo _7	0.014±0.007	0.030±0.009	0.010±0.010	0.000±0.009	0.049±0.024	0.012±0.084	0.0067±0.0058
GdTL_4635	Kowalewo _8	0.032±0.015	0.018±0.008	0.023±0.010	0.025±0.011	0.031±0.018	0.009±0.073	0.0069±0.0056

Table A6a. OSL ages for Baranówko. Dose rate was calculated based on the weighted-mean radioactivity from ICP-MS, μDOSE and HPGe gamma spectrometry.

Lab. Code	Sample ID	Dose rate (Gy·ka^{-1})	Equivalent dose (Gy)	OSL Age (ka)
GdTL_4675	Baranówko_1	1.00±0.04	0.32±0.02	0.25±0.02 MAM
GdTL_4676	Baranówko _2	0.93±0.04	0.34±0.01	0.29±0.02 CAM
GdTL_4677	Baranówko _3	0.89±0.04	0.75±0.02	0.77±0.05 CAM
GdTL_4678	Baranówko _4	0.81±0.04	1.8±0.2	2.1±0.2 MAM
GdTL_4679	Baranówko _5	0.81±0.04	3.0±0.3	3.7±0.4 MAM
GdTL_4680	Baranówko _6	0.87±0.04	4.1±0.2	4.6±0.3 CAM
GdTL_4681	Baranówko _7	0.90±0.04	5.3±0.1	5.8±0.3 CAM
GdTL_4682	Baranówko _8	0.80±0.04	10.7±0.3	13.4±0.8 CAM

Table A6b. OSL ages for Kowalewo. Dose rate was calculated based on the weighted-mean radioactivity from ICP-MS, μDOSE and HPGe gamma spectrometry.

Lab. Code	Sample ID	Dose rate (Gy·ka^{-1})	Equivalent dose (Gy)	OSL Age (ka)
GdTL_4628	Kowalewo_1	1.68±0.05	23.4±0.7	13.9±0.6 CAM
GdTL_4629	Kowalewo _2	1.49±0.05	20.4±0.5	13.6±0.6 CAM
GdTL_4630	Kowalewo _3	1.57±0.05	22.8±0.5	14.4±0.6 CAM
GdTL_4631	Kowalewo _4	1.56±0.05	22.8±0.5	14.5±0.6 CAM
GdTL_4632	Kowalewo _5	1.51±0.05	23.9±0.7	15.7±0.7 CAM
GdTL_4633	Kowalewo _6	1.41±0.05	22.1±0.8	15.6±0.8 CAM
GdTL_4634	Kowalewo _7	1.44±0.05	22.6±0.5	15.7±0.6 CAM
GdTL_4635	Kowalewo _8	1.41±0.04	21.3±0.6	15.0±0.6 CAM

Section B: Radiocarbon Chronology

Table B1. Radiocarbon dates.

Lab. Code	Sample ID	Age ^{14}C (BP)	Age cal BP mean ± s	Age ranges cal BP
GdA-7154.1.1.	Baranówko BRN 1 (90 cm)	623±23	605±30	68.3% probability 650 (31.3%) 625calBP 600 (19.5%) 580calBP 575 (17.5%) 555calBP 95.4% probability 655 (95.4%) 550calBP
GdA-7158.1.1.	Baranówko BRN 5 (200 cm)	3280±26	3500±35	68.3% probability 3560 (21.5%) 3530calBP 3495 (46.7%) 3455calBP 95.4% probability 3565 (95.4%) 3445calBP
GdA-7159.1.1.	Baranówko BRN 6 (240 cm)	4393±27	4955±65	68.3% probability 5030 (9.3%) 5010calBP 4980 (15.7%) 4950calBP 4945 (43.3%) 4875calBP 95.4% probability 5045 (95.4%) 4865calBP
GdA-7160.1.1.	Baranówko BRN 7 (240 cm)	4489±28	5160±80	68.3% probability 5285 (28.2%) 5210calBP 5195 (12.7%) 5160calBP 5140 (15.3%) 5100calBP 5085 (12.1%) 5050calBP 95.4% probability 5295 (93.9%) 5040calBP 5000 (1.5%) 4985calBP

Section C: Automated Mineralogy

Table C1a. QEMSCAN® – mineral composition for Baranówko.

Mineral name	Mineral content (%)							
	BRN_1	BRN_2	BRN_3	BRN_4	BRN_5	BRN_6	BRN_7	BRN_8
Quartz	90.38	90.06	90.82	92.09	89.18	90.12	88.91	91.51
Calcite	0.00	0.00	0.00	0.00	0.00	0.00	0.00	0.00
Dolomite	0.00	0.00	0.00	0.00	0.00	0.00	0.00	0.00
Monazite	0.00	0.00	0.00	0.00	0.00	0.00	0.01	0.00
Apatite	0.00	0.00	0.00	0.00	0.00	0.00	0.00	0.00
Other Phosphates	0.00	0.00	0.00	0.00	0.00	0.00	0.00	0.00
Actinolite	0.02	0.01	0.01	0.02	0.00	0.00	0.13	0.01
Ferrohornblende	0.08	0.05	0.14	0.07	0.20	0.03	0.19	0.04
Hematite	0.12	0.01	0.00	0.00	0.00	0.01	0.01	0.00
Rutile, Anatase, Brookite	0.01	0.05	0.04	0.00	0.06	0.01	0.03	0.01
Titanite	0.00	0.00	0.00	0.00	0.00	0.00	0.00	0.00
Kyanite, Silimanite, Andalusite	0.06	0.01	0.01	0.02	0.01	0.11	0.09	0.13
Ilmenite	0.20	0.06	0.04	0.04	0.10	0.01	0.22	0.06
Zircon	0.05	0.00	0.00	0.04	0.04	0.06	0.03	0.06
Cordierite	0.00	0.01	0.09	0.00	0.00	0.04	0.00	0.00
Staurolite	0.00	0.17	0.00	0.00	0.00	0.00	0.00	0.00
Almandine	0.00	0.10	0.00	0.08	0.01	0.04	0.00	0.00
Pyrope	0.00	0.00	0.00	0.00	0.00	0.00	0.00	0.00
Grossular	0.37	0.01	0.01	0.29	0.14	0.08	0.12	0.08
Calderite	0.00	0.00	0.00	0.00	0.00	0.00	0.00	0.00
K Feldspar	5.26	5.31	5.20	4.66	6.36	5.36	7.15	4.47
Albite	1.65	1.78	1.90	1.53	2.22	2.27	1.70	1.70
Andesine	1.40	1.85	1.49	0.79	1.35	1.55	1.12	1.56
Muscovite/Sericite	0.15	0.21	0.11	0.12	0.15	0.14	0.16	0.13
Biotite/ilmenite/smectite	0.08	0.02	0.01	0.01	0.01	0.01	0.02	0.04
Illite	0.02	0.02	0.01	0.01	0.01	0.01	0.02	0.02
Glauconite	0.01	0.00	0.00	0.00	0.00	0.00	0.00	0.01
Other clay minerals	0.14	0.11	0.12	0.12	0.10	0.11	0.10	0.15
Chamosite Fe chlorite	0.00	0.15	0.00	0.10	0.06	0.05	0.00	0.00
Augite	0.00	0.00	0.00	0.01	0.00	0.00	0.00	0.00
Bronzite	0.00	0.00	0.00	0.00	0.00	0.00	0.00	0.00
Tourmaline	0.00	0.00	0.00	0.00	0.00	0.00	0.00	0.00
Fraction	Fraction content (%)							
< 8 µm	0.19	0.18	0.19	0.14	0.15	0.15	0.17	0.14
8–16 µm	0.41	0.45	0.44	0.31	0.32	0.29	0.36	0.15
16–31 µm	1.08	1.21	1.00	0.78	0.91	0.85	1.00	0.34
31–63 µm	7.06	7.93	6.37	5.60	6.33	6.14	5.91	3.17
63–125 µm	37.67	32.77	31.99	32.89	39.82	36.60	37.18	21.56
125–250 µm	45.66	52.72	48.10	51.93	48.32	52.54	50.32	54.66
250–500 µm	7.93	4.74	10.50	8.35	4.15	3.43	5.06	19.98
>500 µm	0.00	0.00	1.41	0.00	0.00	0.00	0.00	0.00

Table C1b. QEMSCAN® – mineral composition for Kowalewo.

Mineral name	Mineral content (%)							
	KOW_1	KOW _2	KOW _3	KOW _4	KOW _5	KOW_6	KOW _7	KOW _8
Quartz	84.23	80.20	82.65	79.96	80.55	80.77	80.97	79.98
Calcite	1.32	2.94	2.45	3.73	3.60	4.17	2.41	3.77
Dolomite	0.02	1.41	0.73	0.97	1.53	1.26	1.36	1.64
Monazite	0.00	0.00	0.00	0.00	0.04	0.00	0.00	0.00
Apatite	0.20	0.11	0.06	0.12	0.21	0.11	0.17	0.25
Other Phosphates	0.01	0.00	0.00	0.01	0.00	0.01	0.01	0.00
Actinolite	0.27	0.03	0.03	0.21	0.04	0.04	0.12	0.04
Ferrohornblende	0.26	0.02	0.44	0.25	0.27	0.27	0.25	0.13
Hematite	0.19	0.15	0.08	0.15	0.12	0.08	0.07	0.07
Rutile, Anatase, Brookite	0.16	0.07	0.08	0.06	0.11	0.06	0.07	0.03
Titanite	0.00	0.00	0.00	0.02	0.02	0.01	0.00	0.01
Kyanite, Silimanite, Andalusite	0.05	0.03	0.01	0.06	0.01	0.01	0.01	0.06
Ilmenite	0.30	0.24	0.10	0.06	0.25	0.29	0.37	0.08
Zircon	0.09	0.17	0.04	0.20	0.07	0.05	0.09	0.09
Cordierite	0.03	0.04	0.00	0.00	0.00	0.04	0.03	0.01
Staurolite	0.00	0.00	0.00	0.00	0.00	0.03	0.00	0.00
Almandine	0.04	0.01	0.05	0.17	0.00	0.00	0.00	0.02
Pyrope	0.00	0.01	0.00	0.01	0.00	0.00	0.00	0.00
Grossular	0.15	0.03	0.05	0.29	0.26	0.11	0.01	0.06
Calderite	0.00	0.00	0.03	0.00	0.00	0.00	0.00	0.00
K Feldspar	7.10	7.70	7.74	8.45	7.89	7.43	8.00	8.42
Albite	2.23	3.01	2.36	2.01	2.01	1.97	2.41	2.01
Andesine	2.40	2.61	1.79	1.97	1.95	2.17	2.26	2.05
Muscovite/Sericite	0.17	0.13	0.18	0.13	0.17	0.12	0.14	0.14
Biotite/ilmenite/smectite	0.17	0.21	0.23	0.20	0.19	0.27	0.27	0.21
Illite	0.01	0.02	0.03	0.01	0.02	0.02	0.02	0.03
Glauconite	0.26	0.35	0.55	0.41	0.23	0.30	0.55	0.36
Other clay minerals	0.22	0.30	0.25	0.41	0.29	0.35	0.30	0.38
Chamosite Fe chlorite	0.05	0.17	0.03	0.12	0.03	0.01	0.03	0.11
Augite	0.06	0.03	0.01	0.03	0.09	0.03	0.06	0.03
Bronzite	0.00	0.00	0.00	0.00	0.01	0.00	0.02	0.00
Tourmaline	0.01	0.01	0.03	0.00	0.00	0.00	0.01	0.01
Fraction	Fraction content (%)							
< 8 µm	0.19	0.19	0.14	0.20	0.25	0.23	0.18	0.24
8–16 µm	0.53	0.59	0.43	0.57	0.70	0.67	0.57	0.68
16–31 µm	1.87	2.16	1.69	1.87	2.15	2.08	1.94	2.03
31–63 µm	15.18	14.70	13.49	12.80	15.86	13.29	14.77	12.97
63–125 µm	53.65	49.57	51.98	50.65	52.25	57.24	59.87	50.67
125–250 µm	24.79	28.43	25.91	31.50	25.63	25.53	22.67	30.42
250–500 µm	3.79	4.36	6.36	2.41	3.16	0.96	0.00	2.99
>500 µm	0.00	0.00	0.00	0.00	0.00	0.00	0.00	0.00

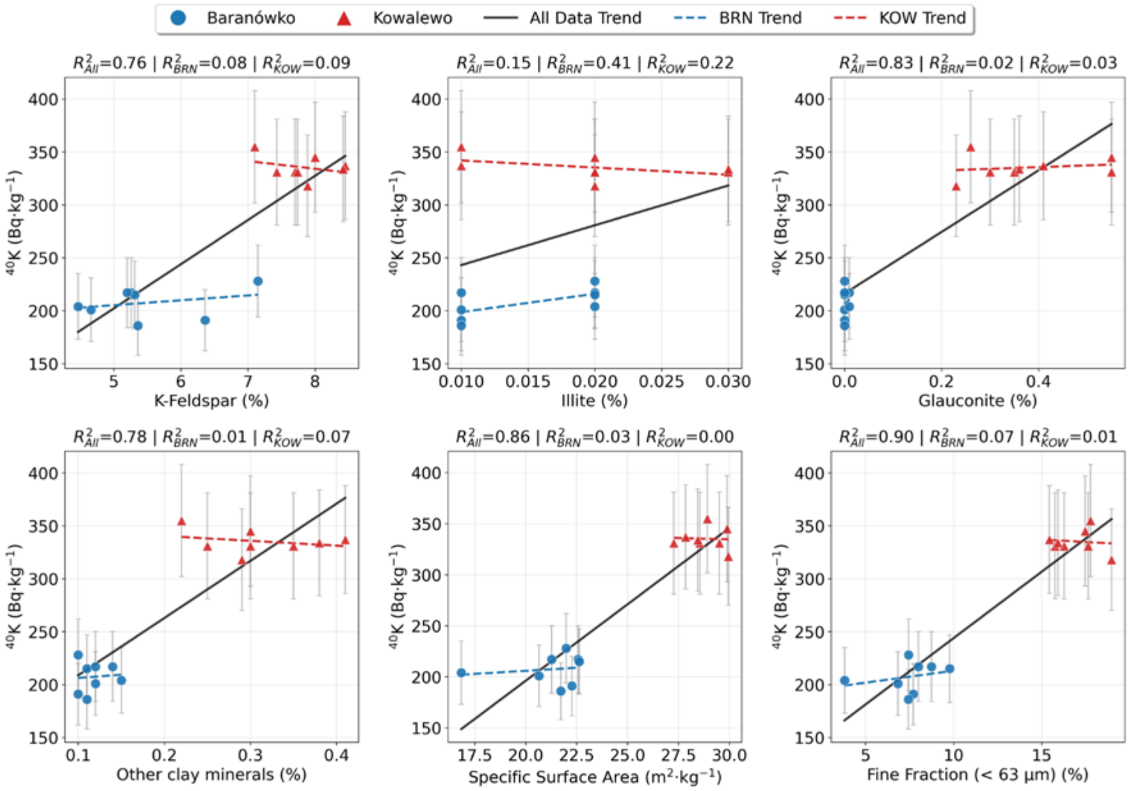

Fig. C2a. Correlation scatter plots illustrating the relationships between ^{40}K activity concentration and selected light/clay mineral carriers (K-feldspar, illite, glauconite, other clays), as well as the physical properties of the sediments (Specific Surface Area and fine fraction <63 µm). Dashed lines indicate local linear regression trends for the Baranówko (blue circles) and Kowalewo (red triangles) sites. The solid black line represents the global regression trend derived from the entire dataset.

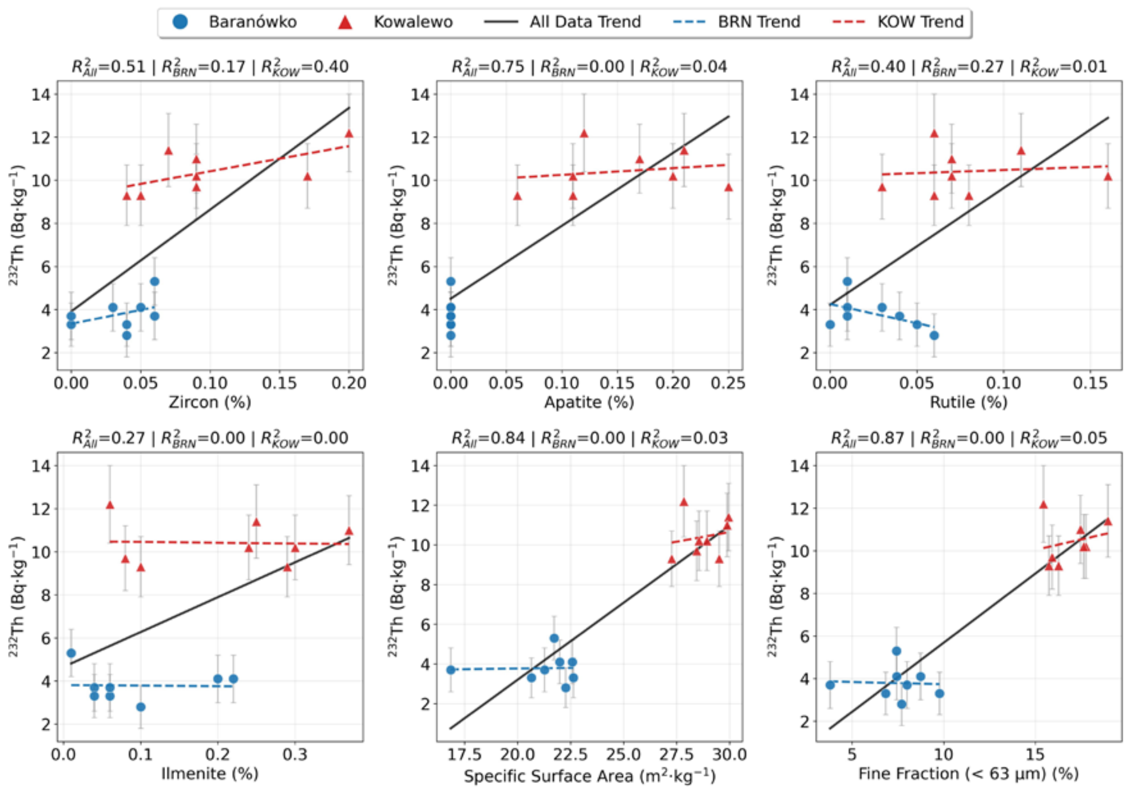

Fig. C2b. Correlation scatter plots illustrating the relationships between ^{232}Th activity concentration and selected heavy mineral carriers (zircon, apatite, rutile, ilmenite), alongside the physical properties of the sediments (Specific Surface Area and fine fraction <63 µm). Dashed lines denote local linear regression trends for the Baranówko (blue circles) and Kowalewo (red triangles) sites, while the solid black line shows the global regression trend for all combined data. Corresponding coefficients of determination (R^2) are displayed above each panel. Error bars represent measurement uncertainties.

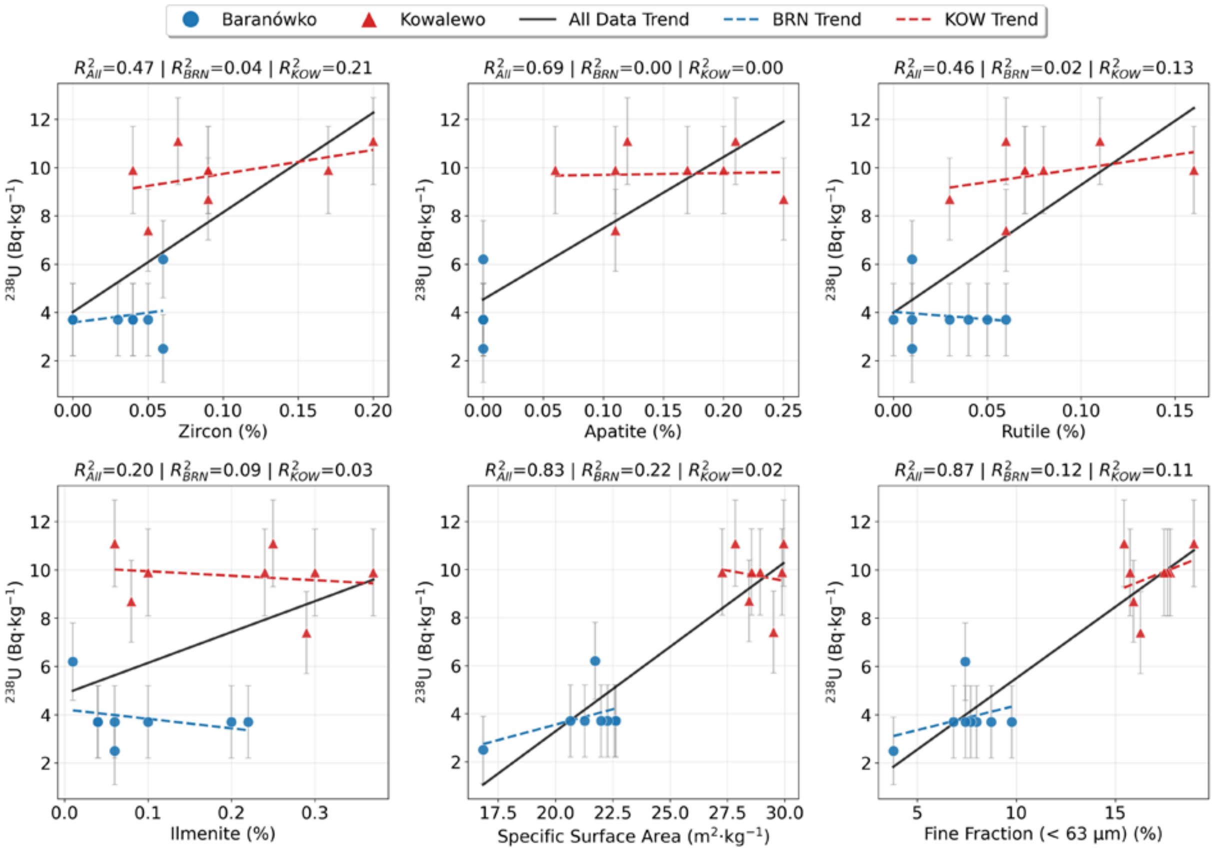

Fig. C2c. Correlation scatter plots illustrating the relationships between ^{238}U activity concentration and selected heavy mineral carriers (zircon, apatite, rutile, ilmenite), as well as the physical properties of the sediments (Specific Surface Area and fine fraction <63 µm). Dashed lines represent local linear regression trends for the Baranówko (blue circles) and Kowalewo (red triangles) sites. The solid black line indicates the global regression trend for the entire dataset. Coefficients of determination (R^2) are provided above each panel to evaluate the strength of these relationships. Error bars represent measurement uncertainties for the radionuclide activity.

Section D: Grain size analysis (Malvern Mastersizer 2000 laser diffraction particle size analyzer)

Table D1a. The changes in grain size distribution of the sample for Baranówko.

Lab. Code	Sample ID	Fraction content (%)						
		<16 µm	16–32 µm	32–63 µm	63–125 µm	125–250 µm	250–500 µm	>500 µm
GdTL_4675	Baranówko_1	1.61	1.59	0.96	16.12	51.3	27.16	1.28
GdTL_4676	Baranówko _2	1.77	1.97	2.48	19.95	47.17	22.5	4.16
GdTL_4677	Baranówko _3	2.62	3.56	5.17	19.48	43.75	21.71	3.74
GdTL_4678	Baranówko _4	1.98	2.23	1.19	13.89	45.11	27.77	7.88
GdTL_4679	Baranówko _5	1.46	1.17	0.47	18.07	52.04	21.84	4.93
GdTL_4680	Baranówko _6	2.23	2.59	2.13	12.28	44.48	28.85	7.45
GdTL_4681	Baranówko _7	2.28	1.43	1.04	21.06	50.54	20.43	3.23
GdTL_4682	Baranówko _8	1.34	0.37	0	3.98	28.62	40.75	24.93

Table D1b. The changes in the median and mean grain size for Kowalewo.

Lab. Code	Sample ID	Φ5 (φ)	Φ16 (φ)	Φ25 (φ)	Φ50 (φ)	Φ75 (φ)	Φ84 (φ)	Φ95 (φ)	Md (φ)	Mz (φ)
GdTL_4675	Baranówko_1	1.19	1.58	1.8	2.31	2.86	3.12	3.76	2.31	2.34
GdTL_4676	Baranówko _2	1.01	1.55	1.83	2.43	3.01	3.31	4.13	2.43	2.43
GdTL_4677	Baranówko _3	1.05	1.58	1.86	2.49	3.17	3.56	5.13	2.49	2.54
GdTL_4678	Baranówko _4	0.75	1.32	1.6	2.2	2.81	3.11	4.06	2.2	2.21
GdTL_4679	Baranówko _5	0.96	1.55	1.83	2.37	2.89	3.13	3.64	2.37	2.35
GdTL_4680	Baranówko _6	0.76	1.33	1.6	2.18	2.79	3.12	4.74	2.18	2.21
GdTL_4681	Baranówko _7	1.11	1.64	1.91	2.47	3	3.27	3.87	2.47	2.46
GdTL_4682	Baranówko _8	0.24	0.71	0.96	1.52	2.13	2.42	3.06	1.52	1.55

Table D2a. The changes in grain size distribution of the sample for Kowalewo.

Lab. Code	Sample ID	Fraction content (%)						
		<16 µm	16–32 µm	32–63 µm	63–125 µm	125–250 µm	250–500 µm	>500 µm
GdTL_4628	Kowalewo_1	1.75	0	3.07	37.4	49.29	6.67	1.83
GdTL_4629	Kowalewo _2	1.11	0	3.76	39.21	48.76	5.93	1.23
GdTL_4630	Kowalewo _3	1.19	0	3.4	42.79	49.56	3.05	0
GdTL_4631	Kowalewo _4	1.1	0	3.11	41.04	50.84	3.89	0
GdTL_4632	Kowalewo _5	0.87	0	2.75	40.18	51.29	4.13	0.77
GdTL_4633	Kowalewo _6	1.35	0	1.61	38.44	55.35	3.22	0
GdTL_4634	Kowalewo _7	0.77	0	1.48	38.71	56.3	2.73	0
GdTL_4635	Kowalewo _8	1.08	0	2.4	40.82	52.7	2.99	0

Table D2b. The changes in the median and mean grain size for Kowalewo.

Lab. Code	Sample ID	Φ5 (φ)	Φ16 (φ)	Φ25 (φ)	Φ50 (φ)	Φ75 (φ)	Φ84 (φ)	Φ95 (φ)	Md (φ)	Mz (φ)
GdTL_4628	Kowalewo_1	1.63	2.16	2.39	2.85	3.29	3.49	3.89	2.85	2.83
GdTL_4629	Kowalewo _2	1.73	2.2	2.43	2.88	3.32	3.52	3.9	2.88	2.87
GdTL_4630	Kowalewo _3	1.98	2.34	2.53	2.94	3.34	3.52	3.88	2.94	2.94
GdTL_4631	Kowalewo _4	1.93	2.3	2.49	2.91	3.32	3.5	3.87	2.91	2.9
GdTL_4632	Kowalewo _5	1.88	2.27	2.47	2.89	3.29	3.48	3.83	2.89	2.88
GdTL_4633	Kowalewo _6	1.95	2.29	2.47	2.86	3.24	3.42	3.78	2.86	2.86
GdTL_4634	Kowalewo _7	1.98	2.31	2.48	2.86	3.22	3.4	3.73	2.86	2.86
GdTL_4635	Kowalewo _8	1.98	2.32	2.51	2.9	3.29	3.47	3.82	2.9	2.9